Shibuya and Sumita
Progress in Earth and Planetary Science (2022) 9:43
https://doi.org/10.1186/s40645-022-00501-7

Progress in Earth and Planetary Science

RESEARCH ARTICLE Open Access

Experiments on seepage-triggered cliff landslides using cohesive wet sand

Fumi Shibuya and Ikuro Sumita*

Abstract

Unsaturated wet sand possesses capillary cohesion that is lost when it becomes saturated. Thus, it can form a cliff, but a slide may be triggered upon saturation. Here we conduct cliff landslide experiments using cohesive wet sand where the groundwater seeps in from the hydraulic head h_w located at the rear of a cliff (height H) and vary these parameters. Importantly, we measure both the total stress σ and pore water pressure u to obtain the effective stress $\sigma' = \sigma - u$. The experiments show that for a fixed H ($\simeq$ 20 cm), a slide is triggered when the h_w exceeds a critical level. The slide occurs nearly simultaneous or after the groundwater seeps out from the cliff toe and the vertical velocity increases approximately exponentially during the slide. As h_w rises, 2 slides are triggered that progress downslope, and for the highest h_w, the whole cliff is pushed forward after the first slide. On the other hand, when the H is high, the slide becomes deep seated. The time needed for the water to seep out from the cliff toe decreases with the h_w and increases with the H, as modeled by a permeable flow with a permeability that decreases with the σ'. The σ_z (vertical) is initially uneven and deviates from the lithostatic value by arching. For tall cliffs, the σ_z near the cliff toe falls precipitously soon after the seepage starts prior to the rise in u, indicating that a stress redistribution occurred as the wet sand loses cohesion and slip plane develops. This also indicates the efficacy of σ measurement because the changes are detected before the groundwater arrives. A stability analysis that models the drop in cohesion and a rise in u explains the cliff becoming unstable with h_w and the slide becoming deep seated with H. However, it overestimates the factor of safety F_s because it does not include the capillary rise and the fall in σ_z.

Keywords: Granular matter, Capillary cohesion, Arching, Groundwater seepage, Cliff landslide, Total stress, Pore water pressure, Effective stress, Permeable flow, Stability analysis

1 Introduction

A rise in groundwater level above an impermeable bedrock is considered to be an important cause for triggering landslides (Whitely et al. 2019). Here the water may be supplied by infiltration from the surface by rainfall and snow melting, from adjacent stream, lake and river (De Blasio 2011; Highland and Bobrowsky 2008), and from a change in groundwater path caused by an earthquake (Morimoto et al. 1967). The landslide processes which follow are complex and the resulting slide morphology is diverse and evolves with time (Allen 1985; Varnes 1978). As a consequence, it is difficult to accurately predict when and how a slide will start, progress, and end. Conversely, this implies that we are still unable to infer the condition that triggered the slide by observing the resulting slide morphology.

When a landslide occurs, the shape of a cliff or a slope evolves with time. The soil, which consists a cliff or a slope, is mainly a wet unsaturated granular matter (a multiphase medium with a complex microstructure), whose rheology varies from solid-like (static, brittle failure, frictional) to fluid-like (viscous flow) (Andreotti et al. 2013). These features of landslides are difficult to model theoretically. Accordingly an experimental approach, which is capable of modeling these features, is needed.

*Correspondence: isumita@staff.kanazawa-u.ac.jp

Earth and Planetary Science Course, Division of Geosciences and Civil Engineering, Graduate School of Natural Science and Technology, Kanazawa University, Kanazawa 920-1192, Japan

The role of experiments is to identify the important physical processes, which are to be included in the theoretical models, and to reveal the parameter dependence and scaling relations.

There have been many landslide experiments conducted in the laboratory and in outdoor flumes. Here the water seeps into an unsaturated granular block or a heap and the processes are monitored by imagery and sensors. The water may be supplied from the adjacent hydraulic head (Berhanu et al. 2012; Fox and Wilson 2010; Fox et al. 2006, 2007; Gregoretti et al. 2010; Lobkovsky et al. 2004; Okeke and Wang 2016; Orense et al. 2004; Tohari et al. 2007), from the base (Iverson et al. 1997, 2000), and by rainfall (Berhanu et al. 2012; Iverson et al. 1997, 2000; Moriwaki et al. 2004; Orense et al. 2004; Tohari et al. 2007). Here we raise 3 issues which have not been addressed sufficiently in the previous landslide experiments, on which we focus in this work.

The first issue is to model landslides triggered by the loss of capillary cohesion with seepage, and to quantify the loss of cohesion and its destabilizing effect. The strength of granular matter is comprised of frictional and cohesive strengths, both of which depend on the water content. Frictional strength falls as the pore water pressure rises because the effective normal stress is reduced. Cohesive strength arising from capillarity is lost when the granular matter becomes saturated, as studied in soil mechanics (Fredlund et al. 2012) and in granular physics (Mitarai and Nori 2006). Cohesion becomes relatively important compared to friction when the normal stress is small, which is the situation for shallow and steep slopes (Iverson et al. 1997), and for slides on planets or satellites with low gravity (De Blasio 2011; Melosh 2011). It is also important for soil consisting of fine particles, such as silt and clay (Whitely et al. 2019), because capillary cohesion scales inversely to the particle size (Andreotti et al. 2013). When the groundwater level rises in a cliff or a slope, which consists of wet granular matter, the cohesion below the phreatic surface is lost, and may cause an instability. Although the importance of the loss of cohesion for triggering slides has been realized (Fox and Wilson 2010; Fukuoka 1980; Krahn et al. 1989), landslide experiments which quantified the destabilizing effect arising from this mechanism are limited (Fox et al. 2007; Tohari et al. 2007). This is partly because the rheology of wet granular matter (the same as that used in the landslide experiments) with variable water content is not routinely measured. Capillary cohesion at intermediate water content is not clearly understood (Mitarai and Nori 2006, Sect. 2), and their measurements are still limited (Fredlund et al. 2012; Matsushi and Matsukura 2006).

The second is measurement of the total stress σ, the vertical component σ_z in particular, which is necessary for 2 reasons. One reason is to evaluate the deviation of σ_z from lithostacy, which affects the stability of a cliff or a slope. Such deviation can arise by arching (stress transfer) which occurs in cohesive soil whose support is partially absent (Terzaghi et al. 1996), when there is a wall (Duran 2000), and when there are soils with different stiffness (Watts and Charles 1988). Another reason is to evaluate the degree of fluidization. Granular matter becomes fluidized when the pore water pressure u balances the σ ($u \sim \sigma$), which occurs when the u rises or when the σ falls. Thus, both the u and σ need to be measured to quantify the degree of fluidization. However, compared to the u, the measurement of σ in the landslide experiments has been scarce (Iverson 1997).

The third is how the morphology and spatial scales of the slide, the time scales needed for the water to seep out from the cliff toe and to trigger a slide, depends on the hydraulic head h_w and the cliff height H. Although previous experiments have varied these parameters (Berhanu et al. 2012; Fox et al. 2006; Gregoretti et al. 2010; Lobkovsky et al. 2004; Okeke and Wang 2016), we do not fully understand how the landslide morphology depend on the h_w and H, when the cohesion is lost below the phreatic surface, and how the characteristic length, time, and σ_z of the landslide, scale as a function of these parameters. For a given h_w and H, we may use theoretical models to estimate the time needed for seepage, the cliff stability, and the geometry of the slip plane. More comparison between experiments and theory is needed to verify and to correct the models.

In this study, we address the 3 issues raised above using unsaturated wet sand, which loses cohesion by an order of magnitude when it becomes saturated; a rheology which we measured. We use a setup with a hydraulic head that is suited to specifically address the effect of the rise in groundwater level. This simple geometry also allows an easier comparison with the theories. We vary the h_w and H, and monitor the whole process of the landslide using video imagery and by measuring the σ, u, and vertical displacement Δz.

This paper is organized as follows. First we explain how the rheology of the wet sand changes with water content. Then we describe the experimental methods and the characteristic scales relevant to our experiments. Next we show the whole time sequence of the cliff landslides using images and sensor measurements where we vary the h_w. Then we show the effects of H (and h_w) on the head length of the slide. We analyze the σ, u, Δz measurements and the images to show how the characteristic scales depend on the H and h_w, which are compared with the theoretical estimates and an empirical relation. Finally, based on the experiments we provide implications for field landslides.

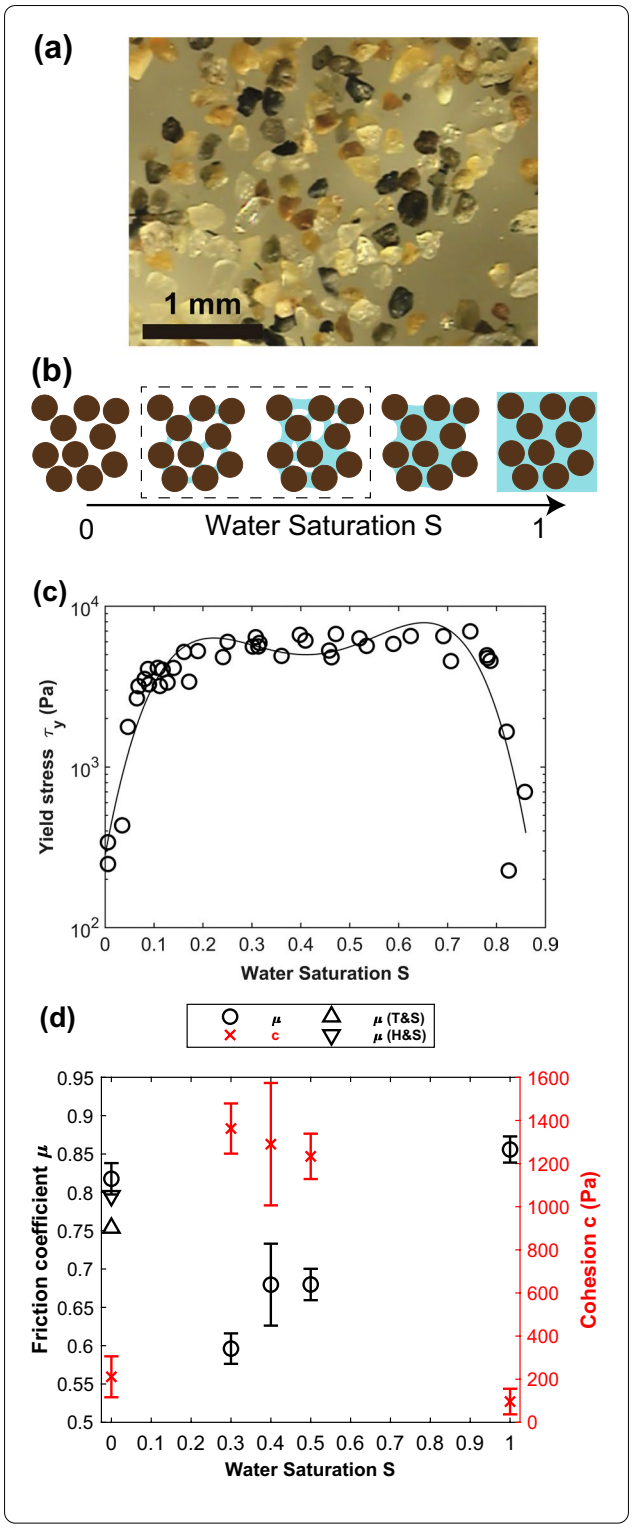

Fig. 1 **a** A photo of the sand particles used for the experiments. **b** A schematic diagram showing the structural change of the wet sand with increasing water saturation S. A box indicates the intermediate S (left: pendular, right: funicular) in which liquid bridges form. **c** Yield stress τ_y versus S ($\phi = 0.50 \pm 0.02$) of the wet sand obtained from vane rheometry. A curve is a fourth-order polynomial fit to $\ln \tau_y$ (Takita and Sumita 2013). **d** Friction coefficient μ (◯: left axis) and cohesion c (×: right axis) versus S of wet sand obtained from parallel plate rheometry (see Additional file 4: Table S1 for the values of μ and c). The μ obtained from the angle of repose θ_r of dry sand ($S = 0$) is also plotted. △: $\mu = 0.75$ from a convex pile (Takita and Sumita 2013), ▽: $\mu = 0.80$ from a concave crater (Hayashi and Sumita 2017)

2 Physical properties and rheology of wet sand

Figure 1a shows the fine beach sand (Chirihama, Japan) used in our experiments. The median particle diameter is $d = 0.204$ mm (25% $d = 0.171$ mm, 75% $d = 0.245$ mm; measured using Shimadzu, SALD-2200J and confirmed via microscope), and the density is $\rho_s = 2610$ kg/m^3 (see Table 1 for the notation). The volumetric packing fraction ϕ of sand and water saturation S [volumetric fraction of water in the pore space $1 - \phi$; Mitarai and Nori (2006)] are used to characterize the volume of sand particles and water (see Additional file 4, for the method to calculate ϕ and S). It follows that the bulk density of the wet sand ρ becomes

$$\rho = \phi\rho_s + S(1-\phi)\rho_w, \tag{1}$$

where the $\rho_w = 1000$ kg/m^3 is the density of water.

Figure 1b is a schematic diagram showing how the structure of the wet sand changes as the water saturation S increases from dry ($S = 0$) to fully saturated ($S = 1$) [modified from Mitarai and Nori (2006)]. In an unsaturated state, liquid bridges and liquid-filled pores exist, which give rise to the cohesion. At the intermediate S (indicated by a box), the S-dependence of cohesion is inconclusive (Mitarai and Nori 2006).

We use 2 methods to measure the rheology of wet sand as a function of S. First we use vane rheometry to obtain the yield stress τ_y (see Additional file 4: Fig. S1 for examples of the time-series data), which we plot as a function of S in Fig. 1c. The figure shows that the τ_y of unsaturated ($S \sim 0.3$) wet sand is $\tau_y \sim 6000$ Pa, which is an order of magnitude larger than the $\tau_y \simeq 230$–700 Pa of the dry ($S \sim 0$) or nearly saturated ($S \sim 0.84$) sand (Mitarai and Nori 2006; Strauch and Herminghaus 2012). At intermediate S, similar to Scheel et al. (2008), the τ_y is insensitive to S. Additional file 4: Fig. S1 also shows that when unsaturated wet sand is sheared, the shear stress τ fluctuates with time, which indicates a stick-slip. Such fluctuation of τ is not observed for dry or saturated sand.

Second, we use parallel plate rheometry to obtain the friction coefficient μ and cohesion c by fitting the shear

Table 1 Notation

A	Growth rate of vertical velocity (1/s)
a	Acceleration (m/s^2)
c	Cohesion (Pa)
c'	Effective cohesion (Pa)
d	Particle diameter (m)
F_s	Factor of safety
g	Gravitational acceleration (m/s^2)
H	Cliff height (m)
H_{max}	Maximum cliff height (m)
h	Height of phreatic surface (m)
h_c	Capillary rise (m)
h_w	Hydraulic head (m)
K_p	Coefficient of passive earth pressure
k	Permeability (m^2)
L	Cliff length (m)
L_{head}	Landslide head length of first slide (m)
S	Water saturation in pore space
T_{seep}	Seepage time (s)
T_{slide}	Slide time (s)
t	Time (s)
u	Pore water pressure (Pa)
v	Velocity (m/s)
W	Cliff width (m)
γ	Surface tension coefficient (N/m)
Δz	Vertical displacement (m)
η	Viscosity of water (Pa s)
θ	Friction angle (°)
Λ	Inverse velocity = $1/v$ (s/m)
μ	Friction coefficient
μ'	Effective friction coefficient
ρ	Bulk density of wet sand (kg/m^3)
ρ_s	Density of sand (kg/m^3)
ρ_w	Density of water (kg/m^3)
σ	Total normal stress (Pa)
σ_z	Total vertical stress (Pa)
σ'	Effective stress (Pa)
τ	Shear stress (Pa)
τ_s	Shear strength (Pa)
τ_y	Yield stress (Pa)
ϕ	Particle volumetric packing fraction

stress τ versus normal stress σ data to the Coulomb's law of friction,

$$\tau = \mu\sigma + c, \tag{2}$$

(see Additional file 4: Fig. S2 and Table S1). The μ is related to the friction angle θ as $\mu = \tan\theta$. Figure 1d shows the obtained μ and c plotted as a function of S. In Fig. 1d, we also plotted the μ of dry sand ($S = 0$), obtained by measuring the angle of repose θ_r (see legend for details), for comparison. The $\mu = 0.82 \pm 0.02$ ($S = 0$) obtained via rheometry is close to the $\mu = 0.80$ obtained from a concave crater and is slightly larger than the $\mu = 0.75$ obtained from a convex sand pile (see Additional file 4: Table S1 legend, for details).

Now we consider the S dependence of the μ and c. Figure 1d shows that the μ and c at intermediate $S = 0.30$–0.53 are smaller and larger, respectively, compared to those of dry ($S = 0$) or saturated ($S = 1$) sand. Similar to the τ_y (Fig. 1c), the $c \sim 1300$ Pa at intermediate S is an order of magnitude larger than the $c \sim 100$–210 Pa of dry or saturated sand. An S-dependence of an opposite sense for μ and c, is consistent with the results of Fall et al. (2014).

The c of the wet sand can be also estimated from the capillary pressure, which pulls the sand particles together. Here the c is given semi-empirically by $c \sim 10\mu(\gamma/d)$ (Scheel et al. 2008), where $\gamma = 0.072$ N/m is the water–air surface tension coefficient. For our wet sand ($S = 0.3$), substituting $\mu \sim 0.6$ and $d = 0.2$ mm, we obtain $c \sim 2200$ Pa, which agrees with the measured $c \sim 1360$ Pa within a factor of 2, verifying the capillary origin of cohesion.

3 Experimental methods

Figure 2 shows the experimental setup consisting of an acrylic box with the gates, wet sand, hydraulic head, and sensors. The front gate is an acrylic plate and is inserted into slot "a" for runs 1–17 and slot "b" for run 18 (Table 2). The back gate is an acrylic frame to which a steel mesh with a cloth is attached, and it is inserted into slot "d". The back gate allows the water to seep in from the constant hydraulic head (h_w) tank. The water in the tank is supplied from a faucet ("in") and a constant h_w is maintained by an overflow ("out").

Sensor pairs consisting of pressure sensor (Kyowa, PGM-02KG) and pore water pressure sensor (Sensez, HWT-001) are attached to the base and side of the box at locations indicated in Fig. 2b. Pressure sensor measures the total stress σ exerted by the wet sand and pore water (see Additional file 4 for the performance check). Pore water pressure sensor is covered by a mesh with an opening of 0.1 mm (smaller than the sand particle diameter $d \simeq 0.2$ mm) and measures the pore water pressure u. From the σ and u, we obtain the effective stress σ' (Sect. 4). A laser displacement sensor (Keyence, LB-01) with a resolution of 0.01 mm is used to measure the vertical displacement Δz of the top surface of the cliff. The measurable Δz is limited to a height range of $\Delta z < 80$ mm owing to the sensor specification. By

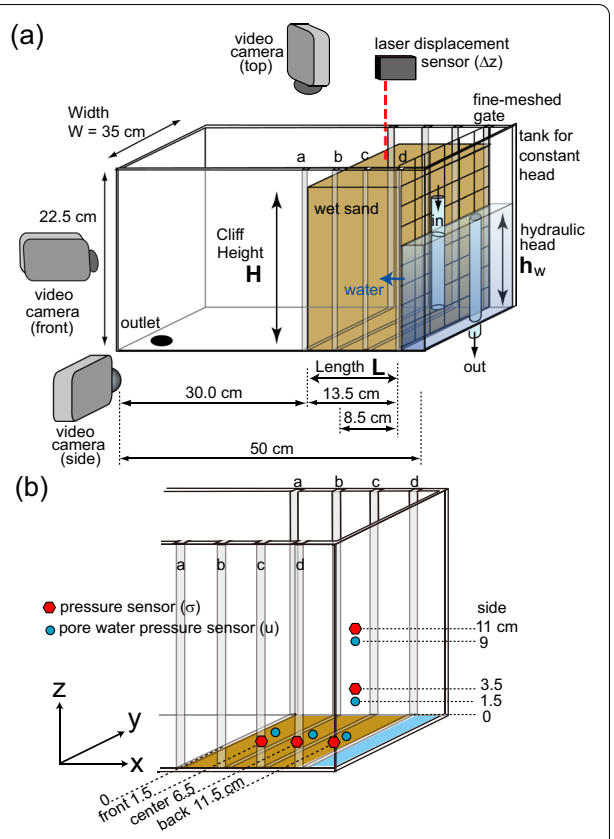

Fig. 2 An experimental setup for cliff landslides. **a** An acrylic box with slots "a"–"d" with a thickness of 1.5 cm for the gates. A laser displacement sensor is positioned above the centerline of the cliff at a distance of ∼ 1.5 cm from the cliff face. **b** Locations of the pressure sensor (measures the σ) and pore water pressure sensor (measures the u) pairs. 3–4 pairs (a total of 6–8) of these sensors are used. The sensors at the bottom (side wall) measures the pressure in the z (y) direction

time-differentiating the Δz, we obtain the vertical velocity v_z. The voltage outputs of these sensors are measured by a multimeter (Agilent, 34970A) at a sampling frequency of ∼ 2 Hz, and the data are recorded by a PC.

The experimental procedure is as follows. First we prepare the wet sand by spraying water onto dry sand and thoroughly mixing them by hand. Next we measure the voltage output of the pressure and pore water pressure sensors under a zero load. Then a cliff is formed by filling the wet sand into the space (length L, height H) between the front and back gates after which the front gate is removed. We take care so that the ϕ of the wet sand is at a constant $\phi = 0.51 \pm 0.01$ (Table 2). This is because the rheology and permeability (Sect. 6.2) of the wet sand depend on the ϕ. Such sensitivity of the landslide rates to ϕ has been documented (Iverson et al. 2000). The S of the wet sand we use is $S = 0.32 \pm 0.08$ (Table 2). The rheology at intermediate S depends little on the S (Fig. 1c, d), from which we estimate that the initial variation of the rheology among the experimental runs is small. Finally, we fill the tank with water to a specified h_w. The tank is filled within ∼ 15 s, which is quick compared to the time required for the water to seep through the cliff (> 49 s, Sect. 5.8). We define the origin time ($t = 0$ s) as when the water level in the tank during filling exceeds $h_w \simeq 1.5$ cm, which is close to the minimum $h_w = 1.8$ cm in our experiments. The whole process of the landslide is recorded by video cameras from 2 or 3 orthogonal directions (Fig. 2a) and synchronized with the sensor measurements using an LED lamp. After the water seeps out from the cliff toe, it spreads and drains from the outlet at the base of the box such that the water level near the cliff toe is maintained at ∼ 6 mm, which was measured from the images. The experimental research reported here was performed with the ethical approval of the Earth and Planetary Science Course, Kanazawa University.

4 Reference scales for the cliff height, stress, and pore water pressure

First we consider the maximum cliff height H_{max} above which it collapses under its own weight. The H_{max} is calculated from the cohesive Mohr–Coulomb criterion (Andreotti et al. 2013) as

$$H_{max} = \frac{2c\cos\theta}{\rho g(1-\sin\theta)}, \tag{3}$$

where ρ is the bulk density [Eq. (1)] and g is the gravitational acceleration. Here, Eq. (3) assumes zero horizontal stress. For our cliff surrounded by 2 side walls and a back gate (Fig. 2a), the obtained H_{max} is a lower-bound estimate because walls stabilize wet granular matter (Nowak et al. 2005). For the $S \sim 0.3$ wet sand which we use to form a cliff, substituting the values for c, θ (Additional file 4: Table S1), and ρ, we obtain an $H_{max} \simeq 33$ cm. The $H_{max} > 20$ cm explains the observation that our initial $H = 20$ cm cliff does not collapse. However, when saturated ($S = 1$), the H_{max} drops to $H_{max} \simeq 2$ cm, indicating that the cliff becomes unstable after seepage. The collapse of a sandcastle (formed by unsaturated sand) due to seepage is a familiar example of such instability. In the shallow region of a cohesive material under extension, a tension crack can form (Bodó and Jones 2013). H_{max} is also the maximum depth which such a crack can form. As above, seepage arrests crack propagation.

For comparison, we also evaluate the H_{max} of natural soils consisting of finer particles. Matsushi and Matsukura (2006) measured the c and θ of unsaturated soils sampled from field slopes around the depth of the slip plane and derived an empirical relation between c and water content. Substituting the parameters for sandy soil

Table 2 A summary of the cliff landslide experiments

Run	H (cm)	H/H_{max}	L (cm)	H/L	ϕ	S	h_w (cm)	h_w/H	Result	Images, movies
1	20.5	0.62	13.5	1.52	0.52	0.31	5.0	0.24	2 slides + spread	–
2	20.0	0.60	13.5	1.48	0.53	0.30	2.0	0.10	No slide	–
3	20.0	0.60	13.5	1.48	0.51	0.55	3.0	0.15	2 slides	–
4	20.0	0.60	13.5	1.48	0.50	0.39	2.0	0.10	1 slide	Fig. 5
5	19.5	0.59	13.5	1.44	0.50	0.33	10.0	0.51	2 slides + spread	–
6	20.0	0.60	13.5	1.48	0.51	0.14	6.0	0.30	2 slides + spread	–
7	20.0	0.60	13.5	1.48	0.51	0.40	15.0	0.75	1 slide + flooding	Fig. 3a
8	20.0	0.60	13.5	1.48	0.50	0.31	2.0	0.10	No slide	Fig. 4
9	12.5	0.38	13.5	0.93	0.49	0.29	2.0	0.16	1 slide†	Fig. 8a
10	12.0	0.36	13.5	0.89	0.51	0.36	2.0	0.17	1 slide	–
11	12.0	0.36	13.5	0.89	0.53	0.29	6.0	0.50	3 slides + spread	–
12	20.0	0.60	13.5	1.48	0.51	0.31	13.0	0.65	1 slide + flooding	Fig. 7 and Additional file 3: Movie S3
13	20.0	0.60	13.5	1.48	0.51	0.37	1.8	0.09	1 slide	Figs. 3a, 8a and Additional file 1: Movie S1
14	20.0	0.60	13.5	1.48	0.50	0.27	8.0	0.40	2 slides + spread	Figs. 3a, 6 and Additional file 2: Movie S2
15	16.0	0.48	13.5	1.19	0.50	0.32	2.0	0.13	No slide	–
16	8.0	0.24	13.5	0.59	0.50	0.28	2.0	0.25	3 slides + spread	–
17	4.0	0.12	13.5	0.30	0.51	0.26	2.0	0.50	1 slide + spread	Fig. 8a
18	12.6	0.38	8.5	1.48	0.51	0.36	5.7	0.45	3 slides + spread	–

H: cliff height, $H_{max} = 33$ cm is obtained from Eq. (3), L: cliff length. The cliff width W is $W = 35$ cm

ϕ: packing fraction of sand particles. Average ± standard deviation: $\phi = 0.51 \pm 0.01$

S: water saturation in pore space. Average ± standard deviation: $S = 0.32 \pm 0.08$

h_w: Hydraulic head. †: sensor data acquisition stopped during the run (× in Fig. 9a)

containing clay and silt into their empirical relation, and assuming $S = 0.3$ (comparable to the initial S of our wet sand), we obtain $c \sim 1.7 \times 10^4$ Pa at $S = 0.3$, which drops to $c \sim 3 \times 10^3$ Pa when it becomes saturated ($S = 1$). Using these values, we obtain $H_{max} \sim 4$ m at $S = 0.3$ and $H_{max} \sim 0.6$ m at $S = 1$. These H_{max} values are an order of magnitude larger than the $H_{max} \simeq 33$ cm, $\simeq 2$ cm for our experiments at the respective S, which can be interpreted as a consequence of a smaller d. This indicates that our experiments can be considered a scaled-down model of the field landslides whose soil consists of clay and silt in addition to sand.

Second, we consider the total stress σ and pore water pressure u, which are used to obtain the effective stress σ' (Terzaghi et al. 1996),

$$\sigma' = \sigma - u. \tag{4}$$

Sand fluidizes ($\sigma' \sim 0$) when the σ falls or the u rises.

For the reference σ, we use σ_0 and $\tilde{\sigma}_0$, which we explain below. σ_0 is the initial σ under lithostacy,

$$\sigma_0 = \rho g H, \tag{5}$$

where H is the cliff height. $\tilde{\sigma}_0$ is the lithostatic σ after the groundwater seeps in and the wet sand becomes saturated to a groundwater level h_w,

$$\tilde{\sigma}_0 = \sigma_0 + \Delta\sigma = \sigma_0 + (1 - S)(1 - \phi)\rho_w g h_w. \tag{6}$$

Here, $\Delta\sigma$ is the stress increase arising from the sand below h_w becoming saturated.

For the reference u, we use the hydrostatic pressure u_0,

$$u_0 = \rho_w g h_w, \tag{7}$$

where h_w is the hydraulic head.

5 Results

Table 2 summarizes the experimental parameters, where we mainly varied the hydraulic head h_w and cliff height H. We also tabulated the dimensionless cliff height H/H_{max} [H_{max}: Eq. (3)], cliff aspect ratio H/L, and the dimensionless hydraulic head h_w/H. These values indicate that the cliff is initially stable ($H/H_{max} < 1$); the cliff aspect ratio varies as $H/L = 0.30$–1.52, thus covering the $H/L \sim 1$; and the h_w/H varies widely as $h_w/H = 0.10$–0.75 in the range limited by $h_w/H < 1$.

In what follows we describe the whole time-sequence of the landslide in detail where we varied the h_w (Sects. 5.1–5.5). Next we show how the landslide head length L_{head} depends on the H (Sect. 5.6). Then we show

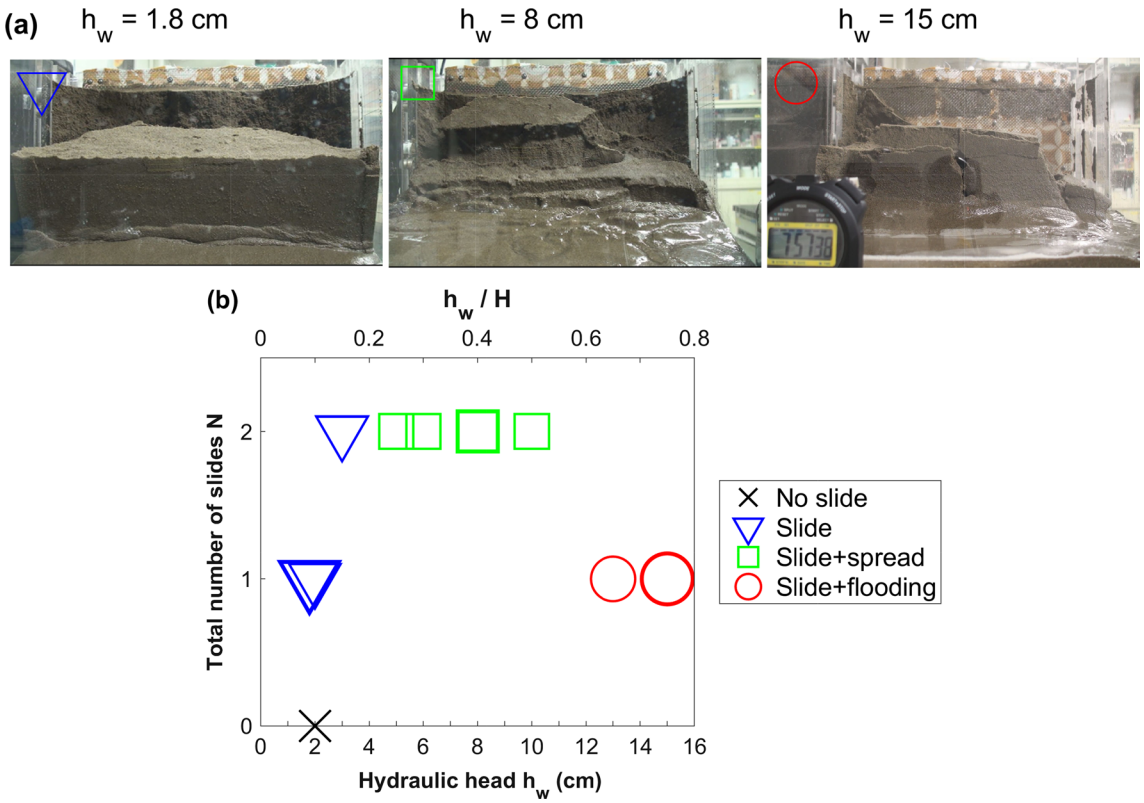

Fig. 3 Hydraulic head h_w dependence of the styles (in marker shapes) and the total number N of the slides of the $H \simeq 20$ cm, $L = 13.5$ cm cliffs. **a** Front views of the landslides at their final stages for three different h_w values. The cliff width is $W = 35$ cm. Left: the $h_w = 1.8$ cm (run 13, $h_w/H = 0.09$, Additional file 1: Movie S1) case at $t = 2940$ s after a slide is triggered. Center: the $h_w = 8$ cm (run 14, $h_w/H = 0.40$, Additional file 2: Movie S2) case at $t = 900$ s after 2 slides are triggered, followed by a spread. The lower (upper) terrace formed after the second (first) slide. Right: the $h_w = 15$ cm (run 7, $h_w/H = 0.75$) case at $t = 180$ s after a slide is triggered, followed by flooding. **b** N versus h_w (a total of 11 runs; there are 2 runs with $N = 0$). The upper horizontal axis is in the h_w/H scale. The 3 large markers correspond to the runs shown in **a**

how the stress and the characteristic time scales depend on the H and h_w, and how the slide accelerates during the slide (Sects. 5.7–5.9).

5.1 An overview of the hydraulic head h_w dependence

Here we describe an overview of the hydraulic head h_w dependence which we varied as $h_w = 1.8$–15.0 cm for a cliff with a fixed height ($H \simeq 20$ cm) and length ($L = 13.5$ cm). This data set forms the majority of our experiments (11 out of 18 runs in Table 2). Figure 3a shows the front views of the 3 runs with different h_w values, and Fig. 3b is a plot showing how the total number of slides N and their styles change with the h_w. At $h_w \simeq 2$ cm ($h_w/H \simeq 0.10$), we have $N = 0 - 1$, indicating that this is the approximate critical h_w above which a slide is triggered. For $h_w = 2$–3 cm ($h_w/H \simeq 0.10$–0.15), the N increases to $N = 2$. We observe that the slides progress in the downslope direction; the second slide is triggered in the slide block that has already slid. For 5 cm $\leq h_w \leq 10$ cm ($0.25 \leq h_w/H \leq 0.50$), after the second slide, a fluidized lateral flow is observed, which we define as a spread (Varnes 1978). For $h_w \geq 13$ cm ($h_w/H \geq 0.65$), after the first slide, the whole cliff translates forward, after which the water flows out, which we define as flooding.

An explanation of the h_w dependent N is as follows. The N increasing from $N = 0$ to $N = 2$ with h_w is a consequence of the cliff becoming unstable with h_w (Sect. 6.3). A second slide is triggered if the cliff which has already slid is still unstable, a condition which is attained at high h_w. For the highest h_w, the N drops to $N = 1$. This is explained by the pressure of the hydraulic head in the rear becoming sufficiently high such that it exceeded the basal friction. In the following sections, we describe the details of the h_w dependence in the order of increasing h_w.

5.2 Case without a slide

Figure 4a shows the top and side views of the $h_w = 2$ cm case (run 8, $h_w/H = 0.10$), and Fig. 4b shows the time-series of the sensor measurements. The images in

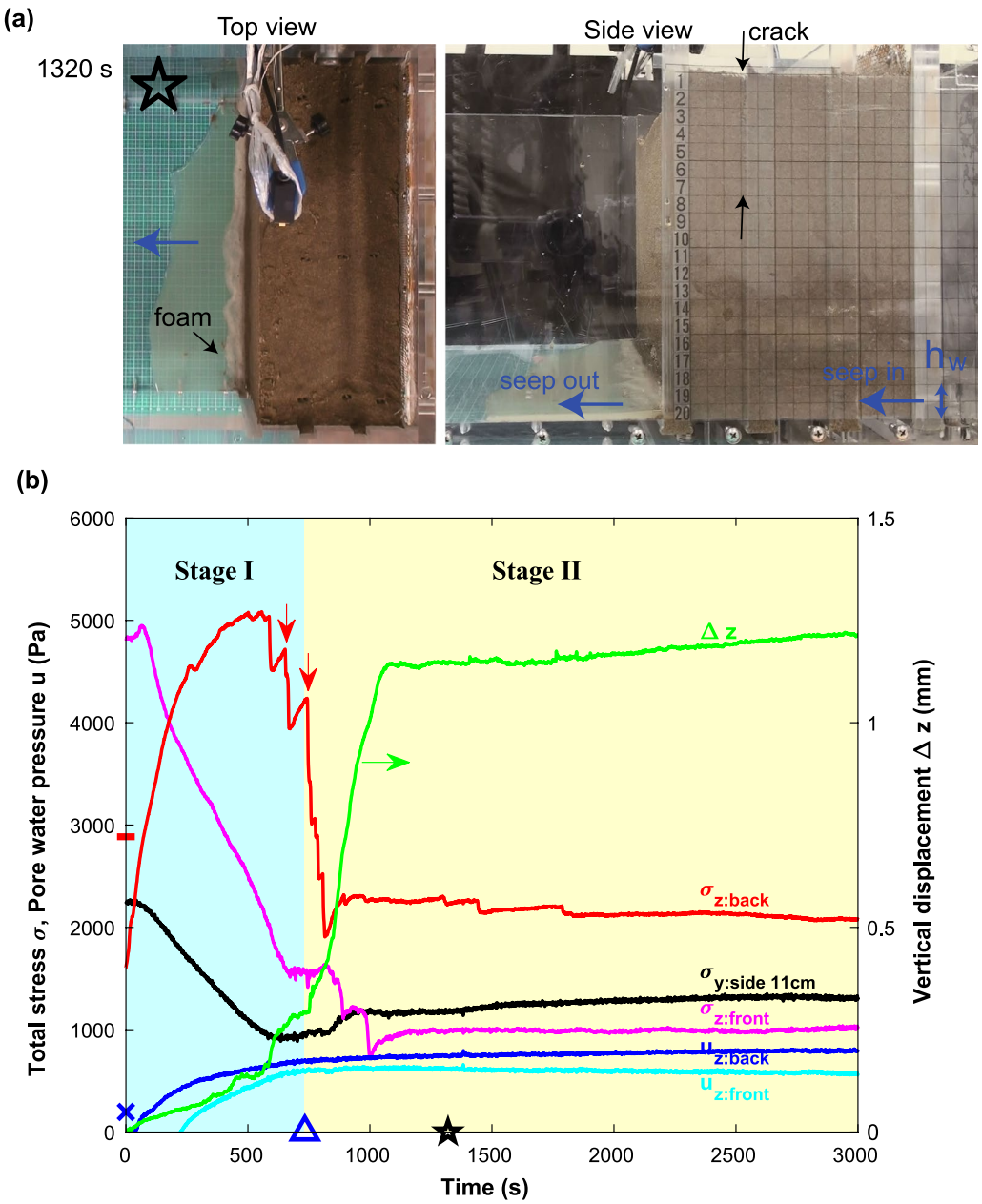

Fig. 4 Results of the $h_w = 2$ cm case (run 8, $H = 20$ cm, $h_w/H = 0.10$), in which no slide is triggered. **a** Images at $t = 1320$ s, and **b** time-series data (5-point running averaged) of total stress σ, pore water pressure u (left axis), and vertical displacement Δz (right axis). Back, front, and side indicate the sensor positions, and subscripts y and z indicate the normal direction (see Fig. 2b). A blue △ is the seepage time T_{seep}, which defines the onset of stage II. A star indicates the $t = 1320$ s when the images shown in **a** were taken. The red vertical bar and blue × (left axis) indicate the reference σ range, $\sigma_0 \le \sigma \le \tilde{\sigma}_0$ [Eqs. (5), (6)], and the $u = u_0$ [Eq. (7)], respectively

Fig. 4a were taken after the water seeped out from the cliff toe. The water that seeped out contains air bubbles that appear to have originated from the air trapped in the pores between the sand particles. In the side view, we observe that a tension crack has formed. However, the crack is not evident in the top view, indicating that its propagation is limited. From the images, we observe that the groundwater seeped out from the cliff toe at $t = 733$ s, which we define as the seepage time T_{seep} (△ on the time axis of Fig. 4b). Using the T_{seep}, we define $0 < t < T_{seep}$ as stage I and $t > T_{seep}$ as stage II, which are indicated in Fig. 4b by the different background

colors. For this run, a slide did not occur after $t = 3000$ s had elapsed, which exceeds $4T_{\mathrm{seep}}$. In another run conducted at the same h_{w} (run 2), a slide did not occur after $3T_{\mathrm{seep}}$ had elapsed. Accordingly, we classified as "No slide" when the slide did not occur after $\geq 3T_{\mathrm{seep}}$ had elapsed.

Now we describe the results shown in Fig. 4b in detail. First we explain the total stress σ and pore water pressure u measurements. We note that at $t = 0$, the σ_{z} measured at the base is uneven, such that near the cliff toe, $\sigma_{\mathrm{z:front}} > \sigma_0$, whereas near the back gate, $\sigma_{\mathrm{z:back}} < \sigma_0$, where σ_0 [Eq. (5)] is the lithostatic value (the minimum of the red vertical bar indicated on the left axis). Such unevenness indicates the effect of lateral support by the back gate. An initially uneven σ_{z} is a common feature of all runs (Sect. 5.7). In stage I, as the water seeps into the cliff, we observe that the $\sigma_{\mathrm{z:back}}$ rises and the $\sigma_{\mathrm{z:front}}$ falls simultaneously. The increase in $\sigma_{\mathrm{z:back}}$ by ~ 3000 Pa is larger by more than a factor of 40 than the estimated rise in $\Delta\sigma = 68$ Pa [Eq. (6)], which is the pressure increase arising from the water that has seeped in. As the water seeps in, first the $u_{\mathrm{z:back}}$ rises, and then the $u_{\mathrm{z:front}}$ rises, as expected from the forward progression of seepage. The $\sigma_{\mathrm{z:front}}$ and $u_{\mathrm{z:front}}$ are measured at the same horizontal distance from the hydraulic head (Fig. 2b). Note that the fall in $\sigma_{\mathrm{z:front}}$ precedes the rise in $u_{\mathrm{z:front}}$, indicating that the $\sigma_{\mathrm{z:front}}$ decreased before the groundwater arrived. These results indicate that the σ distribution within the cliff changed as soon as the seepage started, whose possible mechanism will be discussed in Sect. 6.1. We also note that the $\sigma_{\mathrm{z:back}}$ shows temporal fluctuation (red arrows) indicative of stick-slip, which is similar to that observed when the wet sand is sheared by a vane spindle (Additional file 4: Fig. S1). In stage II, after $t \sim 1000$ s, the σ and u remain approximately constant, indicating a steady-state seepage without a change in σ distribution. At this stage, the $\sigma_{\mathrm{z:front}}$ and $\sigma_{\mathrm{z:back}}$ are both $\sigma_{\mathrm{z}} < \tilde{\sigma}_0$, indicating that the weight of the wet sand is partially supported laterally. We calculate the effective stress σ' from Eq. (4) and find that the $\sigma'_{\mathrm{z:front}}$ decreases precipitously from $\sigma'_{\mathrm{z:front}} \simeq 4840$ Pa at $t = 0$ s to $\sigma'_{\mathrm{z:front}} \simeq 100$ Pa at $t = 1002$ s; a drop by a factor of 48. This indicates that the wet sand has approached fluidization ($\sigma'_{\mathrm{z}} \simeq 0$). Next we consider the vertical displacement Δz. Figure 4b shows that the cliff gradually compacts with seepage until $\Delta z \sim 1.2$ mm at $t \sim 1000$ s, after which the compaction slows down. When the wet sand becomes saturated with water, it loses cohesion and compacts. We confirmed via parallel plate rheometry that the packing fraction ϕ increases by $\delta\phi \sim 0.10$ when the S rises from $S = 0.30$ to $S = 1$ (Additional file 4: Table S1). Using this result, we estimate that a compaction of $\Delta z = 1.2$ mm results when the wet sand with a thickness of 7.3 mm becomes saturated, which is about half of the hydraulic head ($h_{\mathrm{w}} = 2$ cm).

5.3 Case with one slide

Figure 5 shows the result of another run at $h_{\mathrm{w}} = 2$ cm (run 4, $h_{\mathrm{w}}/H = 0.10$). For this case, the water seeps out from the cliff toe at $T_{\mathrm{seep}} = 585$ s, which is comparable to the T_{seep} of the run shown in Fig. 4 within a factor of 1.2. However, after the water seeps out from the cliff toe (stage II), the cliff creeps forward, and tension cracks that initiated near the side walls propagate upward and develop into a horseshoe-shaped crack when viewed from above. Then a deep seated slip plane develops, the slide block tilts forward, and finally a slide is triggered at $t \sim 1500$ s. In another run at $h_{\mathrm{w}} = 1.8$ cm (run 13, see Additional file 1: Movie S1), a slide was triggered at $t \sim 1600$ s. Together with the 2 runs described in Sect. 5.2, a total of 4 runs at $h_{\mathrm{w}} \sim 2$ cm indicate that $h_{\mathrm{w}} = 2$ cm is the approximate critical h_{w} to trigger a slide for a cliff of $H = 20$ cm. The main cause for why slides may or may not be triggered under the same $h_{\mathrm{w}} = 2$ cm is unknown. We consider that it originated from a small difference in the experimental condition which we were unable to control.

Using the vertical velocity v_{z} calculated from the displacement Δz, we define the slide time $T_{\mathrm{slide}} = 1441$ s at the threshold of $v_0 = 0.1$ mm/s, which approximately corresponds to the onset of the accelerated phase of the slide (green ◯ in Fig. 5b). The T_{slide} defines the onset of stage III, which is indicated by the pink background in Fig. 5b. Note that the slide is triggered after the water seeps out from the cliff toe and that the time span of stage II ($T_{\mathrm{seep}} < t < T_{\mathrm{slide}}$) is comparable to the time span of stage I ($0 < t < T_{\mathrm{seep}}$). A compilation of the v_{z}, T_{seep} and T_{slide} for different h_{w} values will be presented in Sect. 5.8.

Next we explain the σ and u measurements. Figure 5b shows that as soon as the water starts to seep into the cliff, the $\sigma_{\mathrm{z:back}}$ rises whereas the $\sigma_{\mathrm{z:front}}$ falls, which is the same as in Fig. 4b. As seepage proceeds, the $\sigma_{\mathrm{z:front}}$ and $u_{\mathrm{z:front}}$ keep falling and rising, respectively, which results in the reduction of the effective stress $\sigma'_{\mathrm{z:front}}$ [Eq. (4)]. In detail, the $\sigma'_{\mathrm{z:front}}$ drops from $\sigma'_{\mathrm{z:front}} \simeq 4860$ Pa at $t = 0$ s to $\sigma'_{\mathrm{z:front}} \simeq 280$ Pa at $t = 738$ s, a drop by a factor of 17.

(See figure on next page.)

Fig. 5 Results of the $h_{\mathrm{w}} = 2$ cm (run 4, $H = 20$ cm, $h_{\mathrm{w}}/H = 0.10$), case in which 1 slide is triggered without a spread. **a** Images, and **b** time-series data of the sensor measurements (5-point running averaged). A blue ⋀ is the seepage time T_{seep}. A green ◯ indicates the Δz (from which v_{z} is obtained) that defines the slide time T_{slide} (the onset of stage III; see text for details). See Fig. 4 legend for explanations of the red bar and blue × on the left axis

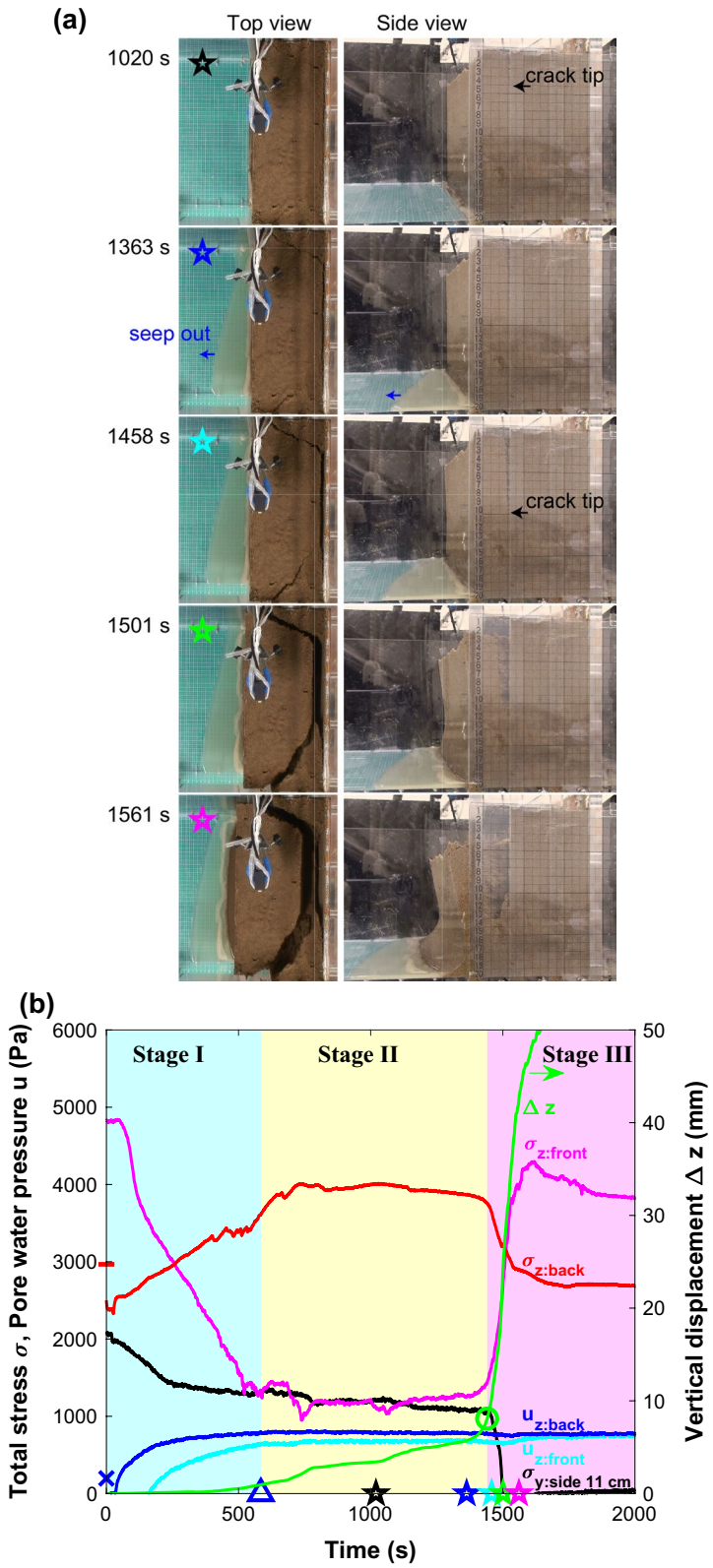

Fig. 5 (See legend on previous page.)

On the other hand after the slide is triggered in stage III, the $\sigma_{z:front}$ rises whereas the $\sigma_{z:back}$ and the $\sigma_{y:side}$ (height 11 cm) fall. From the video images, these changes are inferred to be the result of the cliff detaching from the sidewall and translating forward.

5.4 Case with two slides

Figure 6 shows the results of the $h_w = 8$ cm case (run 14, $h_w/H = 0.40$, Additional file 2: Movie S2). The processes leading to the slide, including the change in σ distribution, are essentially the same as in the case for one slide (Fig. 5). A difference is that for this case, the h_w is sufficiently high to trigger two slides, which progress downslope. As a result, two terraces form where the lower (upper) terrace was formed by the second (first) slide. After the second slide, the cliff toe becomes fluidized and spreads forward. The total stress and pore water pressure measurements show temporal changes similar to those in Fig. 5. We note that in stages I–II, the $\sigma_{y:side}$ at a height of 3.5 cm increases with time. This indicates that the wet sand is being increasingly supported by the side walls as seepage proceeds. The two time scales that characterize seepage and slide are $T_{seep} = 218$ s and $T_{slide} = 308$ s, both of which are shorter than those at a lower h_w (Fig. 5b). The time span of stage II (i.e., $T_{slide} - T_{seep}$) also becomes shorter than that in Fig. 5b.

5.5 Case with one slide followed by flooding

Figure 7 shows the results of the $h_w = 13$ cm case (run 12, $h_w/H = 0.65$, Additional file 3: Movie S3). Similar to Fig. 6, the $\sigma_{z:front}$ falls precipitously during $t \sim 25$–45 s before the $u_{z:front}$ starts to rise at $t \sim 45$ s, and a slide is triggered at $T_{slide} = 54$ s. In contrast, however, after the first slide is triggered, the cliff translates forward, and the water floods out from the constant h_w tank. We also note that the slide is triggered (at T_{slide} plotted as green ◯ in Fig. 7b) 4 s before the water seeps out from the cliff toe (at T_{seep} as blue △). As a result, stage I transitions directly to stage III without stage II.

5.6 *H*-dependent landslide head length L_{head}

Now we show the effect of H on the slide morphology. Figure 8a shows the top views of the runs with 3 different H values where the $h_w \simeq 2$ cm and $L = 13.5$ cm are the same. These images were taken after the first slide was triggered and show that the L_{head} (white arrow) increases with the H; i.e., the slide becomes deep seated. On the other hand, as evident from the images shown in Figs. 5, 6 and 7, the L_{head} varies little with the h_w when the $H \simeq 20$ cm is the same.

We measured the L_{head} and plotted them as a function H in Fig. 8b, where the marker sizes (colors) indicate the h_w. The figure shows that as the H increases, the L_{head} approaches the maximum value limited by the cliff length $L = 13.5$ cm. A comparison with the L_{head} estimated from the stability analysis, which also includes the $L = 8.5$ cm case (run 18), will be given in Sect. 6.3.

5.7 An uneven initial vertical stress σ_z and its temporal change with seepage

Figure 9a shows the compiled result of initial σ_z as a function of cliff height H (H/L). Here the measurements of σ_z near the cliff toe ($\sigma_{z:front}$) and near the back gate ($\sigma_{z:back}$) are classified depending on whether it rises or falls with seepage. In the figure, we added the reference lithostatic σ_0 [Eq. (5)], which separates the super-lithostatic case ($\sigma_z > \sigma_0$, above the line) from the sub-lithostatic case ($\sigma_z < \sigma_0$, below the line). The figure shows that when $H/L \geq 0.59$, the $\sigma_{z:front}$ is super-lithostatic whereas the $\sigma_{z:back}$ is sub-lithostatic and that their difference ($\sigma_{z:front} - \sigma_{z:back}$) increases with H/L. An uneven σ_z that is larger (smaller) at the front (back) can be explained as a consequence of arching, supported by the back gate and facilitated by cohesion (Nowak et al. 2005; Terzaghi et al. 1996). For dry granular matter in a thin rectangular box, it is well known that when H/L exceeds $H/L \sim 1$, we have $\sigma_z < \sigma_0$ (i.e., the Janssen effect) (Duran 2000). The deviation from lithostacy which we observed for tall (large H/L) cliffs suggests a similar origin. For $H/L \geq 0.89$, we find that the $\sigma_{z:front}$ falls, whereas the $\sigma_{z:back}$ rises with seepage, indicating a compensating change as seepage proceeds. On the other hand, at a small H/L, the $\sigma_{z:back} > \sigma_{z:front}$ ($H/L = 0.30$) and the $\sigma_{z:back}$ ($H/L = 0.59$) falling with seepage differ with the results at a larger H/L. It appears that for these small H/L cases, because the effect of arching is less, the initial stress heterogeneity in the cohesive wet sand determines the variation of σ_z.

The fall of $\sigma_{z:front}$ with seepage of tall cliffs is a striking result of our experiments. In Fig. 9b, we compare the $\sigma_{z:front}$ at $t = 0$ and at $t = T_{seep}$ (i.e., when the groundwater seeps out from the cliff toe). The figure shows that for tall ($H/L \geq 0.89$) cliffs, the fall of $\sigma_{z:front}$ is significant such that it becomes sub-lithostatic. We emphasize that if lithostacy holds, then the $\sigma_{z:front}$ should rise with seepage, since $\sigma_{z:front} = \sigma' + u$ [Eq. (4)]. Thus, the fall in

(See figure on next page.)

Fig. 6 Results of $h_w = 8$ cm (run 14, $H = 20$ cm, $h_w/H = 0.40$) case in which 2 slides are triggered, followed by a spread (Additional file 2: Movie S2). **a** Images, and **b** time-series data of the sensor measurements (5-point running averaged). A blue △ is the seepage time T_{seep}. A green ◯ indicates the Δz (from which v_z is obtained) that defines the slide time T_{slide}. See Fig. 4 legend for explanations of the red bar and blue × on the left axis

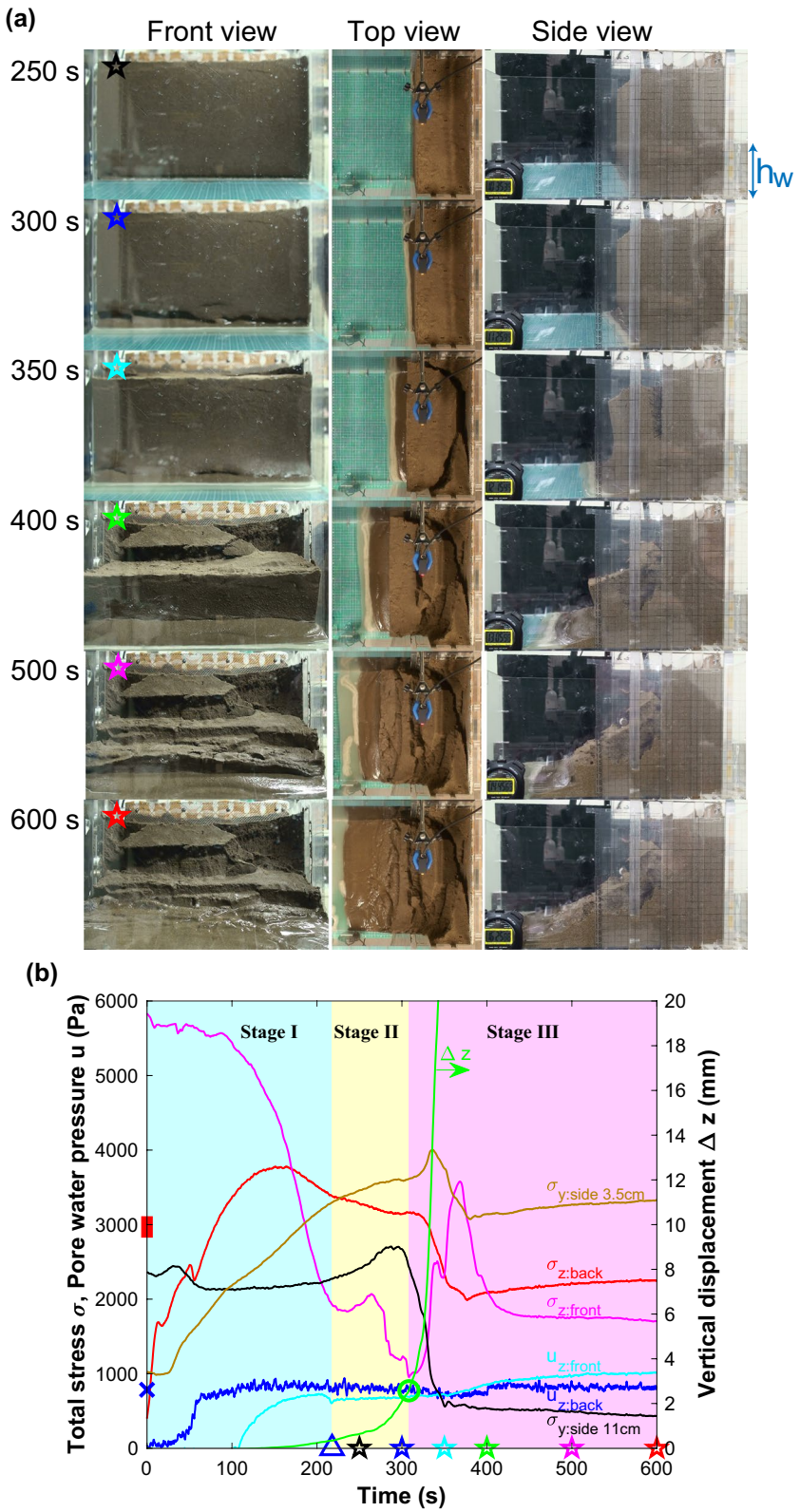

Fig. 6 (See legend on previous page.)

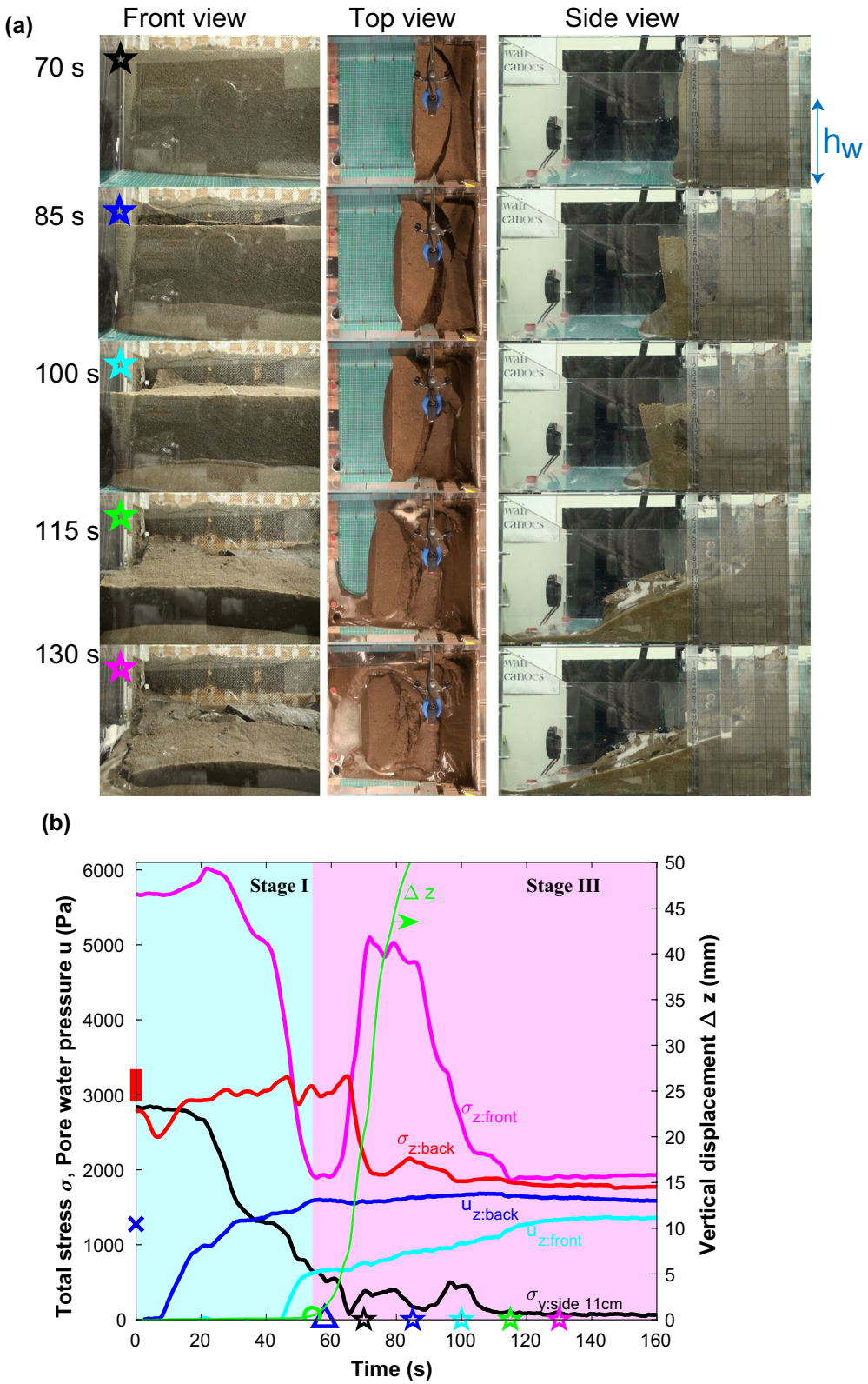

Fig. 7 Results of the $h_w = 13$ cm (run 12, $H = 20$ cm, $h_w/H = 0.65$) case in which a slide is triggered followed by flooding (Additional file 3: Movie S3). **a** Images, and **b** time-series data of the sensor measurements (5-point running averaged). The $T_{slide} = 54$ s (green ◯) and $T_{seep} = 58$ s (blue △) are nearly simultaneous. See Fig. 4 legend for explanations of the red bar and blue × on the left axis

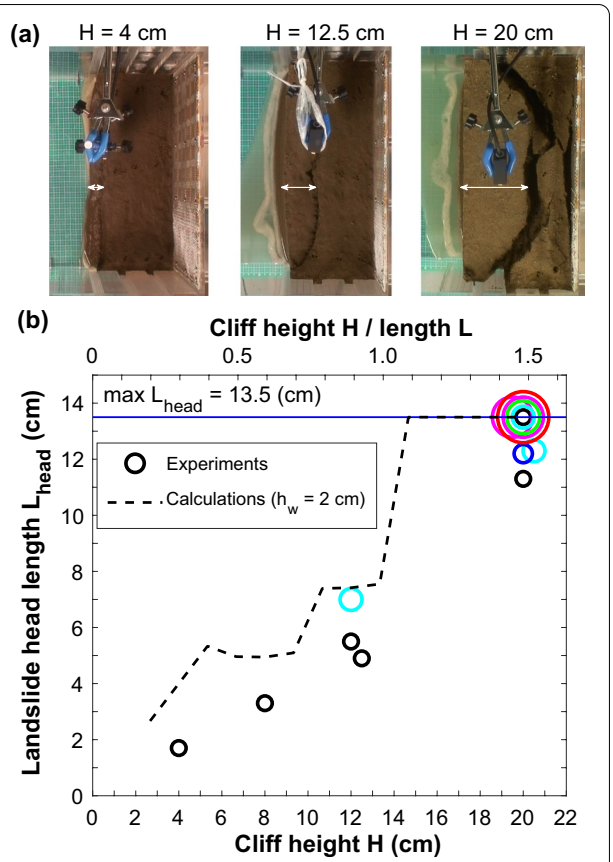

Fig. 8 Cliff height H dependence of the landslide head length L_{head}. **a** Top views after the first slide of the $H = 4, 12.5, 20$ cm cliffs (runs 17, 9, and 13, respectively) with $L = 13.5$ cm and $h_{\text{w}} \simeq 2$ cm. White arrows indicate the L_{head}. **b** L_{head} of the first slide versus H (and H/L), of a total of 14 runs. The size of ◯ corresponds to the h_{w} in the range of $h_{\text{w}} \simeq 2$ cm (smallest ◯ in black) to $h_{\text{w}} = 15$ cm (largest ◯ in red). A black broken line is the L_{head} calculated from the stability analysis for $h_{\text{w}} = 2$ cm. The calculated L_{head} of an $H = 20$ cm cliff depends little on the h_{w} (see text in Sect. 6.3)

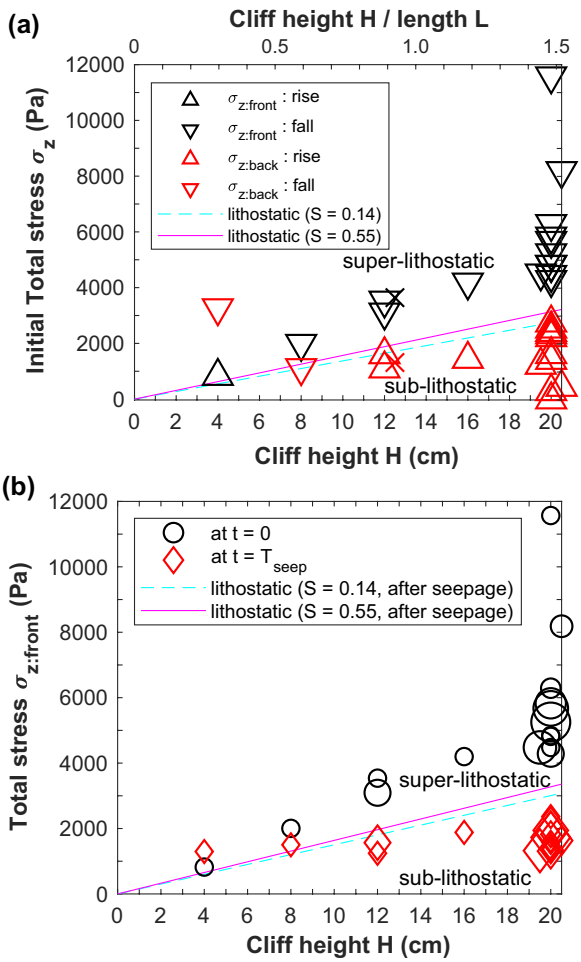

Fig. 9 **a** Initial ($t \simeq 0$ s) total stress σ_{z} versus cliff height H (and H/L) of runs 1–17 in Table 2 ($L = 13.5$ cm). $\sigma_{\text{z:front}}$ and $\sigma_{\text{z:back}}$ indicate the σ_{z} measured near the cliff toe and the back gate, respectively (see Fig. 2b for these locations). △ (▽) indicates the runs in which the rise (fall) in σ_{z} occurred with seepage. × indicates run 9 (see Table 2 legend). A broken (solid) line indicates the lithostatic σ_0 [Eq. (5)] calculated for $\phi = 0.51$and $S = 0.14$ (0.55), which is the minimum (maximum) S in Table 2, and separates the super-lithostatic ($\sigma_{\text{z}} > \sigma_0$) case above and sub-lithostatic ($\sigma_{\text{z}} < \sigma_0$) case below. **b** $\sigma_{\text{z:front}}$ at $t = 0$ s (◯) and at $t = T_{\text{seep}}$ (◇) versus H. The marker sizes correspond to the h_{w}. The lithostatic $\tilde{\sigma}_0$ after seepage [Eq. (6)] was calculated assuming a parabolic phreatic surface with $h_{\text{w}} = 2$ cm. The $\tilde{\sigma}_0$ increases by only a little ($\lesssim 6\%$) for $h_{\text{w}} = 15$ cm

$\sigma_{\text{z:front}}$ indicates that the fall in σ' overwhelms the rise in u. A possible mechanism for this observation will be discussed in Sect. 6.1.

5.8 Time scales for seepage and triggering a slide

Here we show how the 2 characteristic time scales, T_{seep} and T_{slide}, which define the onset of stages II and III, respectively, depend on the h_{w} and H. Figure 10a shows the vertical displacement Δz versus time for different h_{w} values at the same $H \simeq 20$ cm, including the 2 runs without a slide. The slow initial growth of Δz corresponds to the compaction of the cliff prior to the slide. ◯ indicates the Δz at the T_{slide}, which was defined from the threshold velocity $v_0 = 0.1$ mm/s as indicated by ◯ in Fig. 10b. Figure 10b shows the v_{z} of the 9 runs in which a slide was triggered. The figure shows that the v_{z} increases by

2–3 orders of magnitude with time, which we analyze in Sect. 5.9.

In Fig. 10c, we plot the T_{seep} (measured from the images, Sect. 5.2) and the T_{slide} as a function of h_w (at a fixed $H \simeq 20$ cm). The figure shows that both the T_{seep} and T_{slide} decrease with the h_w by a factor of $\simeq 15$ and $\simeq 34$, respectively. The time delay of the T_{slide} relative to the T_{seep} (i.e., the time span of stage II) also decreases with the h_w. In detail, for $h_w = 10$ cm we obtained $T_{slide} - T_{seep} \simeq 14$ s, whereas for $h_w \geq 13$ cm, we obtained $T_{seep} - T_{slide} \simeq 2 - 4$ s (see Additional file 4: Fig. S5 in semi-log to observe that $T_{seep} > T_{slide}$). Thus, at $h_w \geq 13$ cm, the T_{seep} and T_{slide} are nearly simultaneous, and stage II is absent (e.g., Fig. 7). In Fig. 10d, we plot the T_{seep} and T_{slide} as a function of H (at a fixed $h_w \simeq 2$ cm). The figure shows that both the T_{seep} and T_{slide} increase with the H. A model and an explanation of the h_w and H dependences described here will be given in Sects. 6.2 and 6.3 .

5.9 Progressive acceleration of a slide

Figure 11a is a scaled version of Fig. 10b which is a close-up of v_z at around $t = T_{slide}$. A linear trend in semi-log plot suggests an exponential growth of v_z. We fit the data to

$$v_z/v_0 = \exp\left(A(t - T_{slide})\right), \tag{8}$$

where A (1/s) is the growth rate. Here we used the time span of longer than $\simeq 15$ s (≥ 30 data points) such that the relative error $\delta A/A$ is minimized. Figure 11b shows the obtained A plotted versus h_w. A small error bar δA indicates a fair fit to Eq. (8). We find that the A is in the range of $A = 0.03$–0.30 (1/s), and apart from a large A at $h_w = 13.0$ and 15.0 cm, no h_w dependence is found.

Here we also calculate the vertical acceleration a_z and study how it scales with the v_z. Such scaling has been obtained for field landslides in view of forecasting the time of failure which we explain below [see Intrieri et al. (2019) for a review]. Fukuzono (1985) proposed that during a slope failure, the acceleration a scales with the velocity v as

$$a = Av^{\alpha}, \tag{9}$$

and obtained an exponent $\alpha = 1.5$–2.2 from slope failure experiments. He then introduced an inverse velocity $\Lambda = 1/v$ versus time t plot and argued that because $\alpha \sim 2$ corresponds to a linear trend in the $\Lambda - t$ plot, the failure time can be predicted from the intercept with the t axis. Voight (1988, 1989) showed $\alpha \sim 2$ for rockslide and failure of materials, which corresponds to the situation where the crack propagation controls the slip velocity. However, Petley et al. (2002) showed that there are also slides resulting in an asymptotic (non-linear) trend in the $\Lambda - t$ plot that correspond to $\alpha < 2$. He proposed that such slides result from a ductile failure or from slides on an existing slip surface, the former of which was confirmed experimentally by Petley et al. (2005). An $\alpha = 1$ corresponds to the exponential growth [Eq. (8)]. An $\alpha \sim 1$ has been obtained for a surface movement at Mt.Toc, 3 years before the failure (Voight 1988), and for a slide on a structurally stabilized slope (Bozzano et al. 2014). Here we similarly analyze our v_z to obtain the α.

Figure 11c shows the Λ versus t version of the plot shown in Fig. 10b, where we used the time span in the range of $t > T_{slide}$. The figure shows an asymptotic trend similar to those reported by Petley et al. (2002). We note that intermittent decelerating events can be identified indicating a stick-slip behavior. We time-differentiate the v_z to obtain the a_z and plot the a_z versus v_z in Fig. 11d, where we only used the $a_z > 0$ mm/s^2 and $v_z > 0.1$ mm/s data. We fitted the data to Eq. (9) and obtained the power law exponent α. Figure 11e shows the obtained α as a function of h_w. As expected from the asymptotic trend in Fig. 11c, we find $\alpha < 2$ without h_w dependence. The α is scattered around the $\alpha \sim 1$, as expected from an approximate exponential growth shown in Fig. 11a. Here we do not, however, discuss whether the exponential [Eq. (8)] fit (with 1 parameter and a shorter time span) or a power-law [Eq. (9)] fit (with 2 parameters) is suitable. Vane rheometry measurements (Additional file 4: Fig. S1) indicate that when the wet sand becomes saturated, the rheology becomes viscous. We thus infer that the asymptotic trend in the $\Lambda - t$ plot for

(See figure on next page.)

Fig. 10 **a** Vertical displacement Δz versus time (5-point running averaged) of the $H \simeq 20$ cm, $L = 13.5$ cm cliffs. Hydraulic head h_w varies in the range of $h_w = 1.8$–15 cm (numbers annotated). Solid (broken) lines indicate the cases in which the slides were triggered (not triggered). ◯ indicates the Δz at the T_{slide}, which is defined from the threshold velocity v_0 (see **b**). **b** Vertical velocity v_z versus time (5-point running averaged) calculated from **a** using the runs in which a slide was triggered. ◯ indicates the T_{slide} defined at the threshold $v_0 = 0.1$mm/s. **c** T_{seep} (△) and T_{slide} (◯) versus h_w of the $H \simeq 20$ cm cliffs (see Additional file 4: Fig. S5 for a semi-log version). The upper horizontal axis is in the h_w/H scale. Solid and broken curves indicate the T_{seep} calculated by solving Eq. (10) using 2 permeability (k) values: $k_1 = 5.0 \times 10^{-11}$m^2 and $k_2 = 1.8 \times 10^{-11}$m^2. **d** T_{seep}, T_{slide} versus H for a constant $h_w \simeq 2$ cm (see Additional file 4: Fig. S6 for the Δz vs. time plot). There are no measurements of T_{slide} for 4 runs (slide not triggered (3 runs), sensor data acquisition stopped (1 run); see Table 2 legend). The 2 horizontal lines indicate the T_{seep} calculated for $h_w = 2$ cm using the same k_1 and k_2 values used in **c**

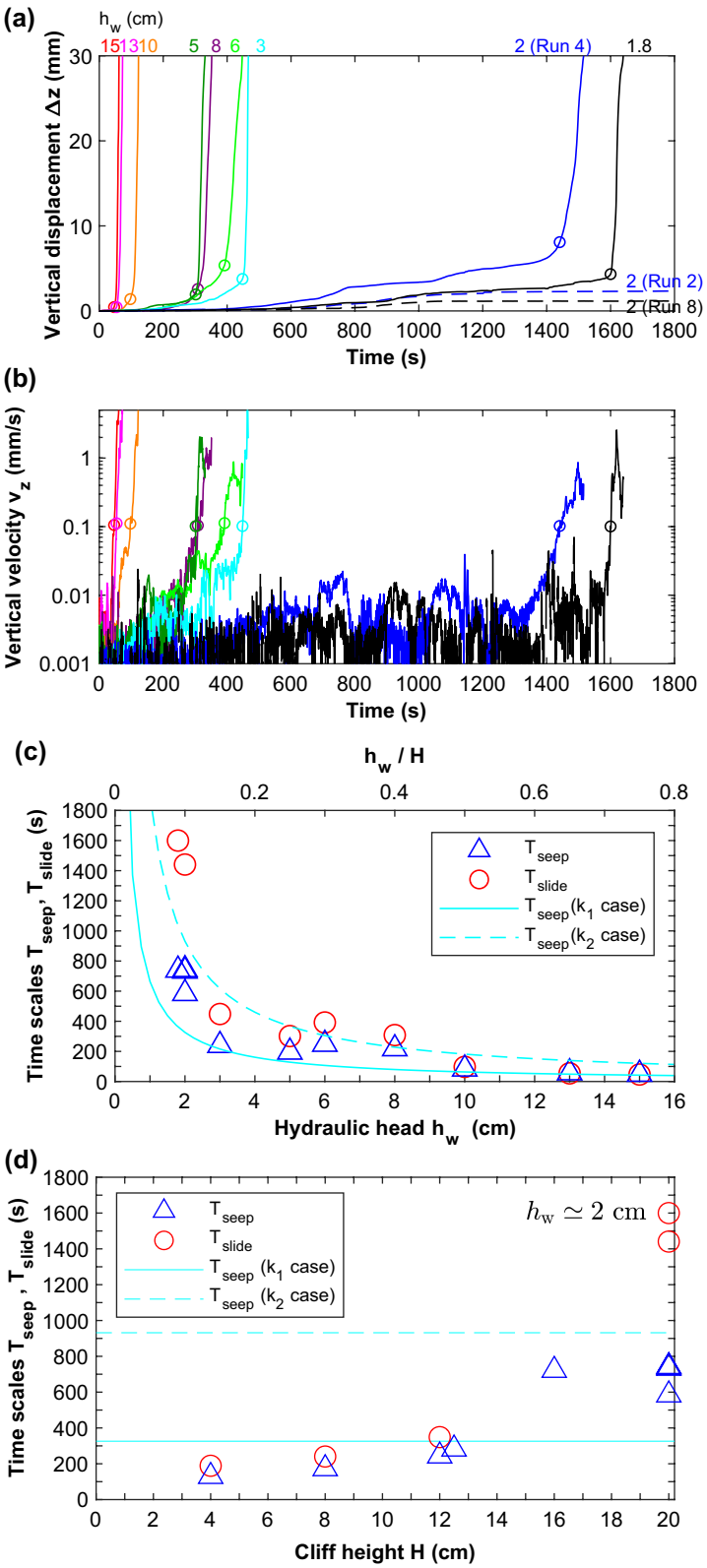

Fig. 10 (See legend on previous page.)

all of our h_w cases can be similarly interpreted as a result of viscous deformation (Petley et al. 2002).

6 Discussions

6.1 Redistribution of effective stress with seepage and the resulting failure

Experiments show that for tall ($H/L \geq 0.89$) cliffs, the $\sigma_{z:back}$ (near the back gate) rises whereas the $\sigma_{z:front}$ (near the cliff toe) falls with seepage (Fig. 9a), and that $\sigma_{z:front}$ becomes sub-lithostatic at $t = T_{seep}$ (Fig. 9b). The rise in $\sigma_{z:back}$ cannot be explained by the rise in u alone. The fall in $\sigma_{z:front}$ starts prior to the rise in u, measured at the same horizontal distance from the hydraulic head, indicating that the groundwater has not yet arrived. These observations indicate a redistribution of effective stress σ', arising from a change in arching, that is related to the loss of cohesion with seepage and the development of the slip plane.

Figure 12a is a schematic diagram showing the stress change inferred from the measurements. The figure models the situation shown in Fig. 6 with $H = 20$ cm and $h_w = 8$ cm. At $t = 0$ s, the $\sigma_{z:front}$ is super-lithostatic whereas the $\sigma_{z:back}$ is sub-lithostatic, indicating an arching. At $t \sim T_{slide}$, we observe that tension cracks formed near the cliff top, indicating that an active failure by horizontal extension occurred. Tension cracks form because cohesive wet sand resists tensile stress σ (< 0) estimated to be $\sigma > -c/\mu \sim -2300$ Pa ($S = 0.3$) (Andreotti et al. 2013). Such cracks only form near the cliff head, above the phreatic surface, as we showed from Eq. (3). On the other hand, near the cliff toe, we infer that the sand is compressed horizontally by the pressure of the hydraulic head, such that a passive failure occurred. This stress pattern is consistent with that inferred from field landslides, where extension and compression features form at the head and toe, respectively (Whitely et al. 2019), and a slip plane which is steeper at the head (Carson 1971; Matsukura 2008); a consequence of steeper failure angle (measured from the horizontal) under tension, compared to that under compression (Fig. 12a, right).

The pattern of σ' in granular matter is commonly described using force chains or networks (Andreotti et al. 2013; De Blasio 2011). Figure 9a suggests that at $t = 0$ s, near the cliff toe the force chains are directed vertical, whereas near the back gate they are directed toward the back gate. Such enhanced wall-effect for unsaturated granular matter, compared to saturated granular matter, has been shown by Nowak et al. (2005). When seepage starts from the rear of the cliff, the cohesion below the phreatic surface drops which we consider weakens the force chains directed toward the back gate. We infer that the force chain redirection toward the base contributed to the rise in $\sigma_{z:back}$. The fall in $\sigma_{z:front}$ occurs simultaneously with the rise in $\sigma_{z:back}$, from which we infer that this is also a result of the force chain redirection. A possible explanation is that the force chains near the cliff toe redirected toward the side walls (in the y-direction), as a consequence of horizontal compression (in the x-direction, see Fig. 12a right). Such redirection toward the wall, perpendicular to the direction of imposed stress, is a property of granular matter as imaged by photoelasticity (Duran 2000). We infer that this redirection supported the weight of the wet sand and thereby reduced the σ_z. Indeed a complementary increase of σ_y measured at the side wall (at a height 3.5 cm) is evident in stages I–II of Fig. 6b. Here the σ_y rises with seepage, exceeding the expected rise from the u. We also note that the $\sigma_{z:front}$ recovers and rises in stage III as evident in Figs. 5b, 6b and 7b. We infer that this stress recovery is a consequence of the cliff detaching from the side walls which weakened the force chains directed in the y-direction.

A consequence of the fall in $\sigma_{z:front}$ is that it promotes failure near the cliff toe, which we explain below. Figure 12b shows the effective Mohr's circle representation of the passive failure condition in the $x - z$ plane near the cliff toe at $t = T_{slide}$ of Fig. 12a. Here we compare the following 2 cases. The first is when the σ_z is at a lithostatic value. From $\sigma_0 \simeq 3109$ Pa [Eq. (6)] and $u \simeq 784$ Pa [Eq. (7)], we obtain the $\sigma'_z \simeq 2325$ Pa [Eq. (4)]. From the Mohr's circle, we obtain $\sigma'_x \simeq 11616$ Pa (coefficient of passive earth pressure $K_p = \sigma'_x/\sigma'_z \simeq 5.0$) for a failure to occur. The second is when we use the measured $\sigma_z \simeq 953$ Pa ($< \sigma_0$), and $u \simeq 688$ Pa at $t = T_{slide} \simeq 308$ s, from which we obtain $\sigma'_z \simeq 265$ Pa. From the Mohr's circle, we obtain $\sigma'_x \simeq 1838$ Pa ($K_p \simeq 6.9$) for a failure to occur. Comparing the σ'_x values for these 2 cases, we find that the σ'_x for the experimental case is reduced to $\sim 16\%$ of the lithostatic case. This shows that the fall in $\sigma_{z:front}$ promotes failure.

6.2 A permeable flow model for seepage

Here we model seepage and calculate the T_{seep} and compare it with the measured T_{seep} shown in Fig. 10c, d. We assume a permeable flow driven by a horizontal pressure gradient (the Dupuit approximation), whose velocity is determined by Darcy's law (Bear 1972; Turcotte and Schubert 2014). We use this simple model which assumes 1-D

(See figure on next page.)

Fig. 11 **a** A scaled version of Fig. 10b with the exponential [Eq. (8)] fits (broken lines). T_{slide} is defined at the threshold $v_0 = 0.1$ mm/s. **b** Growth rate A obtained from the fits in **a** plotted versus hydraulic head h_w. **c** Inverse velocity ($\Lambda = 1/v_z$) versus $t - T_{slide}$ version of Fig. 10b. **d** Acceleration a_z versus velocity v_z (see text for details). The marker colors correspond to the h_w shown in **c**. A line indicates a power-law fit [Eq. (9)] to the $h_w = 10$ cm case (△) from which we obtain a power-law exponent $\alpha = 1.1 \pm 0.1$. **e** α versus h_w obtained from the power-law fits

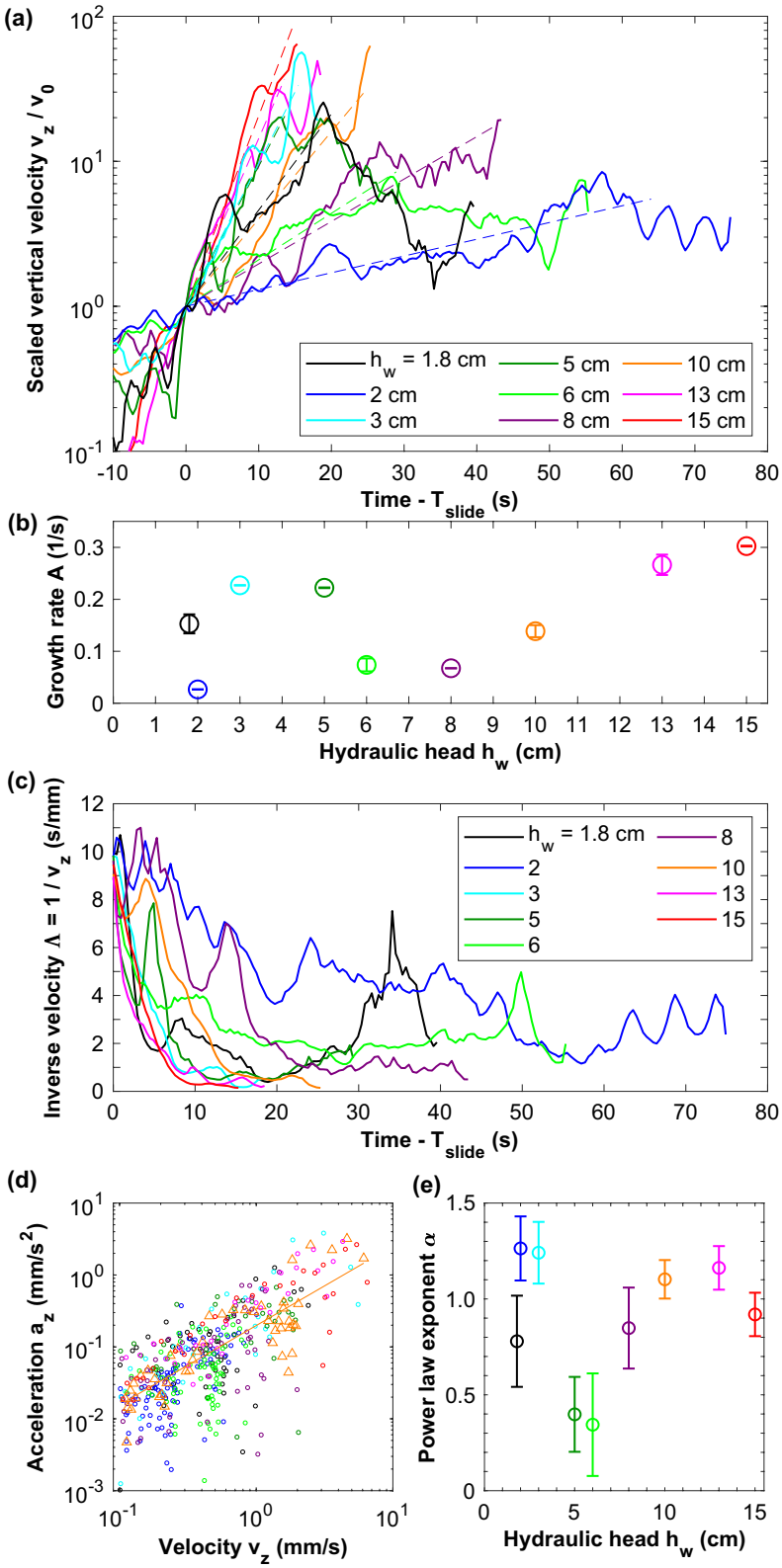

Fig. 11 (See legend on previous page.)

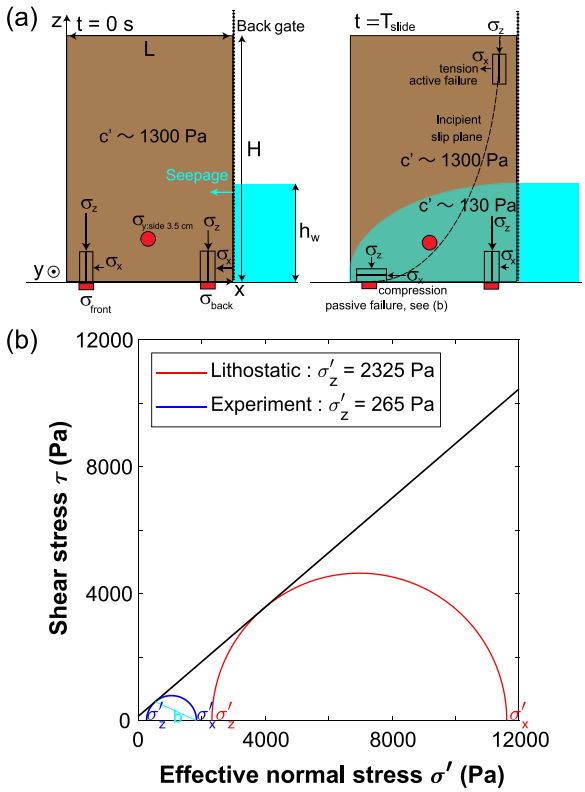

Fig. 12 **a** A schematic diagram to scale showing the inferred stress changes with seepage. The long axis of a rectangle indicates the major principal stress σ, defined positive when the arrow is directed inward. The figure models the situation of run 14 ($H = 20.0$ cm, $L = 13.5$ cm, $h_w = 8$ cm shown in Fig. 6). A red square (circle) indicates the pressure sensor attached to the base (side wall) and measures the σ_z (σ_y). Left: at the beginning of seepage ($t = 0$ s). Right: at $t = T_{slide}$. Near the cliff head, σ_z is the inferred major principal stress, such that active failure (horizontal tension, $\sigma_x < 0$) occurs and a tension crack forms. At the cliff toe, the σ_x is the inferred major principal stress, such that passive failure (horizontal compression, $\sigma_x > 0$) occurs. The failure angle is steeper at the head (see text). **b** Effective Mohr's circle representation of a passive failure at the cliff toe shown in **a** right. A black line is the Mohr–Coulomb criterion for saturated ($S = 1$) sand (see Additional file 4: Table S1 for μ', c'). $b \simeq 25°$ is the failure angle measured from the horizontal for the experimental case

(horizontal) flow because our goal is to clarify whether a simple model can explain the measured T_{seep} and its h_w -dependence. The nonlinear diffusion equation, which governs the height $h(t, x)$ of the phreatic surface, is expressed as

$$\frac{\partial h(t,x)}{\partial t} = \frac{k\rho_w g}{\eta(1-\phi)}\frac{\partial}{\partial x}\left(h(t,x)\frac{\partial h(t,x)}{\partial x}\right), \tag{10}$$

where k is the permeability, $\eta = 1.0 \times 10^{-3}$ Pa s is the viscosity of water at 20 °C, and x is the horizontal coordinate measured from the origin ($x = z = 0$) defined at the cliff toe. For k we use the Kozeny–Carman formula (Bear 1972; Mavko et al. 2019),

$$k = \frac{(1-\phi)^3 d^2}{K\phi^2}, \tag{11}$$

where K is an empirical constant that depends on the particle shape and tortuosity (the ratio of the total flow-path length to the sample length). Previous works have suggested $K = 180$ for spherical (Bear 1972), and $K = 4000$ for aspherical particles (McKenzie 1984). For the ϕ and d we use $\phi = 0.51$ (Table 2) and $d = 0.2$ mm. The initial condition is $h = 0$ cm in the cliff ($0 < x < 13.5$ cm) and the boundary condition is $h(t, x = 13.5\ \text{cm}) = h_w$ at the constant hydraulic head. We numerically integrate Eq. (10) until the water seeps out from the cliff toe. The seepage time T_{seep} is defined when $h(t, x = 0\ \text{cm})$ at the cliff toe exceeds the d.

First we consider the h_w dependence shown in Fig. 10c. We calculated the T_{seep} by varying the h_w using 2 values of k, $k_1 = 5.0 \times 10^{-11}$ m^2 and $k_2 = 1.8 \times 10^{-11}$ m^2, so that the calculated T_{seep} (cyan curves in Fig. 10c) bound the measured T_{seep} (blue △). The curves explain the h_w dependence well (see also Additional file 4: Fig. S5 for a semi-log version). To evaluate whether these values for k are reasonable, we calculated k using Eq. (11) by substituting $\phi = 0.51$, $d = 0.2$ mm, and using $K = 180$ and $K = 4000$ as cited above, and obtained $k = 1.0 \times 10^{-10}$ m^2 and $k = 4.5 \times 10^{-12}$ m^2, respectively. This range of k overlaps k_1 and k_2, indicating that their values are physically reasonable.

Next we consider the H dependence shown in Fig. 10d. The T_{seep} increasing with H suggests that k decreased with H. The k depends on both ϕ and K [Eq. (11)]. The initial ϕ does not depend on H (Table 2), and although the ϕ increases by 0.15–0.75% through compaction during seepage (Additional file 4: Fig. S6), no systematic H dependence is found. Here we note that effective stress $\bar{\sigma}'_z$, which is averaged horizontally (using $\sigma'_{z:front}$, $\sigma'_{z:back}$), and over a time span of $0 < t < T_{seep}$, increases with H (Additional file 4: Fig. S7), as expected from lithostacy. Thus, we infer that the total flow-path length (the tortuosity, hence K) increased with $\bar{\sigma}'_z$ (hence H), because the sand particles were in a closer contact, and that this resulted in the k to decrease.

Darcy's law, used in Eq. (10), assumes a laminar flow (Bear 1972; Turcotte and Schubert 2014). Here we evaluate whether this assumption holds by calculating the Reynolds number $Re = \rho_w \bar{v}_x d/\eta$, where $\bar{v}_x$ is the time-averaged seepage velocity. Using an upper bound of $\bar{v}_x \sim 3$ mm/s, which is the fastest case with $h_w = 15$ cm (run 7), we obtain an upper bound estimate of $Re \sim 0.6$.

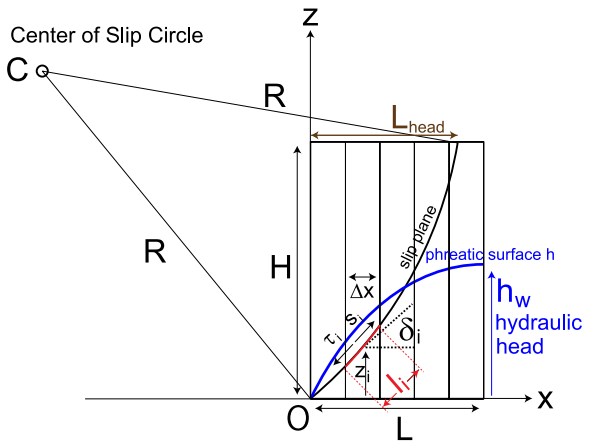

Fig. 13 A schematic diagram showing the geometry of the method of slices used to evaluate cliff stability. The slip plane is circular (center C, radius R), passing through the origin (O). The landslide head length L_{head} is measured from the intercept of the slip circle at the top or rear plane of the cliff. The phreatic surface $h(x)$ is parabolic, such that $h(0) = 0$ and $h(L) = h_{\mathrm{w}}$. Wet sand is saturated (unsaturated) below (above) the $h(x)$, and corresponding values of ρ, μ', c' are used. Δx (= 1.35 mm) is the slice width. z_i, l_i, and δ_i are the height, length, and slope angle of the slip plane, respectively, at the slice number i. s_i and τ_i are the resisting and disturbing tangential stress, respectively, at the slip plane

A value of $Re < \mathcal{O}(1)$ validates assuming a laminar flow (Bear 1972) for the seepage in our experiments.

We note, however, that the flow assumed here is simplified because it neglects the vertical flow. The flow becomes 2-D when when dh/dx becomes of the order of unity (Turcotte and Schubert 2014), which is realized at the front of the phreatic surface. Vertical flow is also driven by suction. Here the resulting capillary rise h_{c} scales as $h_{\mathrm{c}} \propto \gamma/(1-\phi)\rho_{\mathrm{w}} g d$, and using an empirical formula in Terzaghi et al. (1996), we estimate to be around $h_{\mathrm{c}} \sim 10$ cm. A fair agreement with the measurements, despite neglecting the vertical flow, may be because the T_{seep} was measured at the cliff toe, just above the impermeable base, where the vertical velocity approaches zero.

6.3 Comparison with stability analysis

Here we evaluate the cliff stability and estimate the geometry of the most unstable slip plane, and compare them with the experiments. Same as in Sect. 6.2, we use a simple model to clarify the extent of explaining the experiments, which we consider is meaningful before seeking more complex models. Such analysis in conjunction with the experiments has been conducted previously (Fox et al. 2007; Tohari et al. 2007) which we compare with our result at the end of this section.

We use the standard method of slices (Bodó and Jones 2013; De Blasio 2011; Terzaghi et al. 1996) as shown schematically in Fig. 13. We assume a circular slip plane passing through the cliff toe and a parabolic phreatic surface $h(x)$ (Dupuit parabola), which is a solution for a steady flow with a boundary condition $h(x = 0\ \mathrm{cm}) = 0$ cm (Bear 1972; Turcotte and Schubert 2014). A rationale for assuming a circular slip, which is steeper at the head, is because it is consistent with the horizontal tension (compression) at the cliff head (toe) of the landslides (Sect. 6.1). A factor of safety F_{s} is defined as $F_{\mathrm{s}} = M_{\mathrm{R}}/M_{\mathrm{D}}$, where M_{R} is the resisting moment and M_{D} is the disturbing moment for a given slip plane. Thus, the cliff is unstable (stable) when $F_{\mathrm{s}} < 1$ ($F_{\mathrm{s}} > 1$).

M_{R} and M_{D} are evaluated as follows. The cliff is divided into vertical slices, each with a width of Δx. The height, length, and slope angle of the slip plane at each slice are defined as z_i, l_i, and δ_i, respectively, where i is the slice number. The resisting and disturbing tangential stresses at each slice are defined as s_i and τ_i, respectively. F_{s} is then expressed as (Bodó and Jones 2013),

$$F_{\mathrm{s}} = \frac{M_{\mathrm{R}}}{M_{\mathrm{D}}} = \frac{\sum s_i l_i}{\sum \tau_i l_i} = \frac{\sum \left\{ c'_i l_i + (w_i \cos\delta_i - u_i l_i)\mu'_i \right\}}{\sum w_i \sin\delta_i}. \tag{12}$$

Here $w_i = \rho_i g (H - z_i)\Delta x$ is the weight of wet sand (H: cliff height) evaluated at height z_i, and u_i is the pore water pressure. We assume that the wet sand is unsaturated (saturated) above (below) the phreatic surface (height h_i), such that the u_i is zero (non-zero: $u_i = \rho_{\mathrm{w}} g (h_i - z_i)$). Thus, we use $\rho_i = 1488$ kg/m^3, $\mu'_i = 0.60$, and $c'_i = 1362$ Pa ($S = 0.3$ case) above the h_i, and $\rho_i = 1821$ kg/m^3, $\mu'_i = 0.86$, and $c'_i = 133$ Pa below the h_i (Additional file 4: Table S1). We vary the center C of the slip circle (and the circle radius R), and determine the C which minimizes the F_{s}. An example of such calculation is shown in Fig. 14a. From the slip circle, we determine the landslide head length $L_{\mathrm{head}} (\le L)$ as shown in Fig. 13. The calculation is repeated for different pairs of h_{w} ($\le H$) and H to study how the F_{s} and L_{head} depend on these 2 parameters.

Now we compare the calculations with the experiments. First we consider the F_{s}. Figure 14b shows that F_{s} decreases with h_{w}, which is consistent with the existence of a critical h_{w} above which a slide is triggered. Here we demonstrate that the order of magnitude drop in c upon saturation is important. For the $h_{\mathrm{w}} = 12$ cm, $H = 20$ cm case shown in Fig. 14a, if we assume that the c remains unchanged at its unsaturated value below the phreatic surface, then we obtain $F_{\mathrm{s}} = 2.14$, a factor of ~ 2 larger than the $F_{\mathrm{s}} = 0.99$ (red ◯ in Fig. 14b) obtained, which included the drop in c. The calculated critical $h_{\mathrm{w}} \simeq 12$ cm for a slide to be triggered, however, is overestimated compared to the critical $h_{\mathrm{w}} \sim 2$ cm of the experiments.

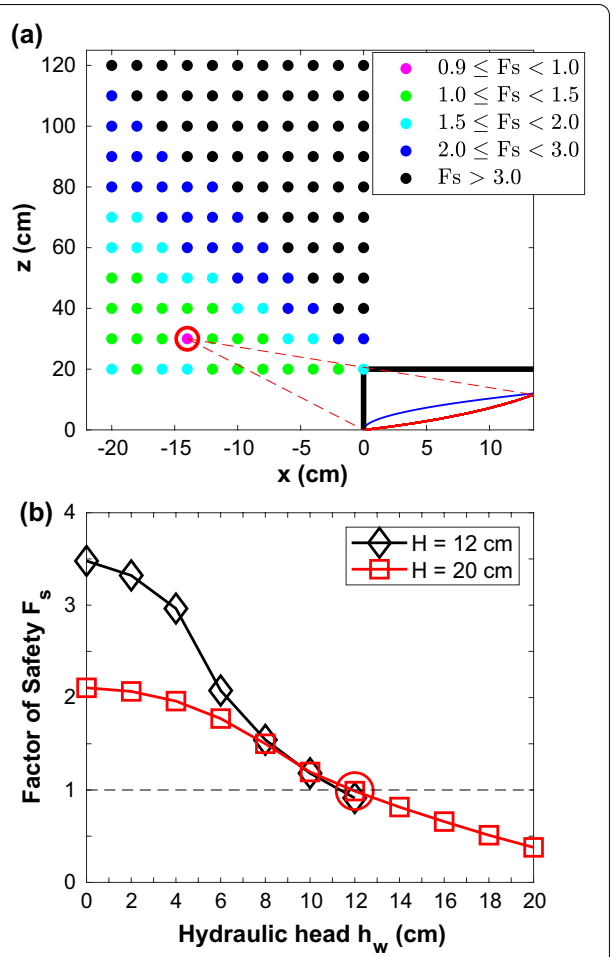

Fig. 14 **a** An example of a factor of safety F_s calculation in which the center of slip circle (C) is varied. A black rectangle indicates the cliff ($H = 20$ cm, $L = 13.5$ cm). A blue curve indicates the phreatic surface with a hydraulic head $h_w = 12$ cm at $x = 13.5$ cm. Filled circles indicate the C, and their colors represent the calculated F_s (see legend for their values). A red circle indicates the C at which the F_s is the minimum ($F_s = 0.99$). Broken red lines are the slip circle radii, and a red arc is the slip circle sector. **b** F_s versus h_w calculated for cliffs with 2 different H values (see legend). For each H, the h_w is varied in the range of $h_w \leq H$. A red ◯ corresponds to the minimum F_s in **a**

We consider that there are 2 main reasons for this discrepancy, both of which overestimate the M_R in Eq. (12). First is the neglect of capillary rise, estimated to be around $h_c \sim 10$ cm (Sect. 6.2), which causes the cohesion c_i of the wet sand above the assumed phreatic surface, to fall. Second is the neglect of $\sigma_{z:front}$ becoming sub-lithostatic near the cliff toe at $t \sim T_{seep}$, which promotes failure (Fig. 12b). In the analysis, lithostacy was assumed, which overestimates the w_i (hence frictional resistance) near the cliff toe where the δ_i is small.

Next we consider the L_{head}. In Fig. 8b, we indicated the L_{head} calculated by varying the H for constant $h_w = 2$ cm and $L = 13.5$ cm. The figure shows that the calculated L_{head} increases with H (i.e., the slide becomes deep seated), in accord with the experiments. We also calculated the L_{head} by varying the h_w at a constant $H = 20$ cm, and find $L_{head} = 13.5$ cm for $h_w \leq 18$ cm, indicating that the L_{head} depends little on the h_w, which also agrees with the experiments. Furthermore, we compared the measured and calculated L_{head} for the $L = 8.5$ cm case (run 18) and found $L_{head} = 8.5$ cm for both. Our analysis thus shows that F_s is overestimated, whereas the L_{head} increasing with H agrees with the experiments.

Here we also interpret the result shown in Fig. 10c (also Additional file 4: Fig. S5), where the time delay $T_{slide} - T_{seep}$ (i.e., the time span of stage II: $T_{seep} < t < T_{slide}$) becomes longer when the h_w is lower. During stage II, we observe that the sand compacts (Figs. 5b, 6b). We consider that this is a consequence of the sand becoming increasingly saturated. When the wet sand becomes saturated ($S = 1$), it loses capillary cohesion (Fig. 1d), and compacts under its own weight, which was verified from rheometry conducted under an imposed normal stress (see legend of Additional file 4: Table S1). When the h_w is low, the cliff becomes stable (Fig. 3b, consistent with large F_s at small h_w in Fig. 14b). A longer time delay can be interpreted as a result of extra time needed for the wet sand to become saturated, not only below the phreatic surface but also above it by capillary rise (so that the F_s decreases), to trigger a slide. On the other hand when the h_w is high, the cliff becomes unstable. A slide can be triggered at $t \sim T_{seep}$, without a further increase in S.

Finally, we compare with previous works. Tohari et al. (2007) conducted landslide experiments triggered by rainfall and groundwater rise and showed that the F_s is overestimated unless the loss of strength by saturation below the tension crack was included, a result similar to ours. Fox et al. (2007) conducted experiments in which groundwater ($h_w/H = 0.86$) seeps into a quasi 2-D bank (cliff and slopes), consisting of sand. They found that the seepage erodes the bank toe and forms an undercutting for steep slopes, after which they collapse, a result broadly similar to our experiments, but different in detail. They compared the slip geometry of the experiments with that obtained from the stability analysis and showed that the analysis could not predict the failure geometry at small slope angles because the slip becomes non-circular.

6.4 Implications for field landslides and their caveats

Now we discuss the implications for field landslides from the perspective of the 3 main issues which we addressed in this work. First, we consider the loss of cohesion c, by an order of magnitude, with seepage. The c and H_{max} [Eq. (3)] of soil consisting of silt and clay, which are finer

compared to the sand we use, also drops by an order of magnitude with S (Sect. 4). Thus, we consider that our experiments are applicable to field landslides whose soil consists of fine particles, and those which are shallow and steep, or at low-gravity (Sect. 1). We note that wet snow is similarly cohesive (Bartelt et al. 2015) and loses cohesion by an order of magnitude when its water content increases (Kamiisi et al. 2009). Thus, snow avalanches triggered by seepage or melting may also share similarities with our experiments.

Second we consider the measurements of total stress σ, which are less common than the measurements of pore water pressure u. We found that the initial σ_z of a tall cliff deviates from lithostacy (Fig. 9a), becoming high near the cliff toe and low near the back gate, and that lithostatic assumption is one reason for the factor of safety F_s being overestimated (Fig. 14b). σ_z has been measured in the field (Watts and Charles 1988) but less commonly compared to the horizontal σ (Araiba and Suemine 1998; Askarinejad et al. 2018; Brackely and Sanders 1992; Cislaghi et al. 2019). Our experiments show that for cohesive soils, one should be cautious about assuming lithostacy and therefore it is meaningful to measure σ_z. We showed that σ_z monitoring detects stress redistribution before the groundwater arrives. This suggests that the σ_z may be used for an early warning, thus complementing the geodetic (Δz) monitoring and the $\Lambda - t$ plot (Fig. 11c).

Third, we consider the h_w and H dependence of the landslides. Our regime diagram (Fig. 3b) for $H \simeq 20$ cm showed that diverse slides occur when the h_w rises. The slide morphology includes 2 slides that progress downslope, spread, translation and flooding, which are not modeled by a standard stability analysis which assumes a slide with a simple geometry that occurs once. This result alerts that one should also consider the stability of the block that has already slid and the possibility of a basal slip. We found that the slide is triggered nearly simultaneous or after the groundwater seeps out from the cliff toe (Fig. 10c), an observation that may be used to constrain the lower limit of T_{slide}. We showed that the T_{seep} is well explained using permeable flow velocity calculated using the permeability k formula in Eq. (11), indicating its applicability whenever direct measurement of k is not possible. We also showed that the T_{seep} increases with H (Fig. 10d), which we explained as a result of k decreasing with the effective stress σ'. This effect needs to be included when one seeks to improve the accuracy of estimating the seepage velocity and hence T_{slide}. We also add that when the soil consists of fine particles, in order to improve the estimate of F_s, one needs to include the capillary rise h_c and an uneven σ_z, latter of which is likely to be enhanced by cohesion.

Finally, we note the caveats of applying the experiments to field landslides. The first is the effect of friction, which scales in proportion to the σ_z and, hence approximately to the H. This means that the small H in our experiments compared to field landslides disproportionately amplified the effect of cohesion (Iverson 2015), when the particle size consisting the cliff is the same. The experiments are not perfectly scaled models of field landslides. The second is the cliff geometry, whose height H to length L, and width W ratios were restricted in the range of $H/L = 0.30$–1.52 and $H/W = 0.11$–0.59. It is possible that this geometry, amplified the effect of arching and contributed to the σ_z deviating from lithostacy. The third is the stepwise increase of h_w at $t \sim 0$ s, and the presence of an impermeable, smooth, rigid base. These conditions were suited to model seepage using a simple permeable flow model (Sect. 6.2), but nevertheless, it was simplified.

7 Conclusions

Experiments on seepage-triggered cliff landslides using unsaturated wet sand were conducted to understand the instability arising from an order of magnitude loss of cohesion c below the phreatic surface, which causes the cliff to become rheologically layered. Diverse styles of slides were revealed as the hydraulic head h_w was raised at a fixed cliff height of $H \simeq 20$ cm. When the h_w is above critical, a slide is triggered (at $t = T_{slide}$), which is simultaneous or after the groundwater seeps out from the cliff toe (at $t = T_{seep}$), where the effective stress σ' is drastically reduced. During the slide, its velocity accelerates approximately exponentially with time which, based on previously obtained empirical laws, suggests viscous deformation. At a higher h_w, 2 slides are triggered that progress downslope, accompanied by a spread. For the highest h_w, the whole cliff translates forward after the first slide and a flooding occurs. On the other hand when the H is high, the slide becomes deep seated (a larger L_{head}). A stability analysis which includes a drop in c and a rise in pore water pressure u, explains the existence of critical h_w above which a slide is triggered and the L_{head} increasing with the cliff height H. However, it overestimates the factor of safety F_s because capillary rise and deviation from lithostacy were not included in the analysis. This result also indicates the necessity to consider the stability of the cliff which has already slid. The T_{seep} decreases with the h_w and increases with the H, which are well modeled by a permeable flow using Kozeny–Carman formula for permeability k, that includes an additional effect of k decreasing with the σ'. For tall ($H/L \geq 0.59$) cliffs, the total stress σ_z near the cliff toe is initially super-lithostatic but drops precipitously with seepage, prior to the rise in u, inferred to be a consequence of the cliff toe (head) being compressed

(extended) horizontally. This drop of σ_z, in addition to the rise in u, contributes to the drastic reduction of σ' at the cliff toe. These results caution assuming lithostacy, a priori, and also suggests the efficacy of σ_z monitoring because precursory changes are detected before the groundwater arrives.

Supplementary Information

The online version contains supplementary material available at https://doi.org/10.1186/s40645-022-00501-7.

Additional file 1: Movie S1. A movie from run 13 (hydraulic head $h_w = 1.8$ cm, cliff height $H = 20$ cm, $h_w/H = 0.09$) replayed at $\times 50$ speed. The movie starts at $t = 740$ s when the groundwater seeps out from the cliff toe after which a slide is triggered. A photo of this run is shown in Fig. 3a.

Additional file 2: Movie S2. A movie from run 14 ($h_w = 8$ cm, $H = 20$ cm, $h_w/H = 0.40$) replayed at $\times 10$ speed. The movie starts at $t = 218$ s when the groundwater seeps out from the cliff toe after which 2 slides are triggered which progress down slope followed by a lateral spread. Photos of this run are shown in Figs. 3a, 6a.

Additional file 3: Movie S3. A movie from run 12 ($h_w = 13$ cm, $H = 20$ cm, $h_w/H = 0.65$) replayed at $\times 2$ speed. The movie starts at $t = 58$ s when the groundwater seeps out from the cliff toe after which a slide is triggered followed by flooding. Photos of this run are shown in Fig. 7a.

Additional file 4. Additional material on the method for calculating ϕ and S, rheometry, performance check of pressure sensor, and addenda on the h_w, H dependences.

Acknowledgements
We thank the 2 anonymous reviewers whose comments helped to improve the manuscript, A. Namiki, N. Endo, K. Kashiwaya for discussions and technical support.

Authors' contributions
FS designed the apparatus, conducted the experiments and vane rheometry. IS contributed to setting up the apparatus and conducted parallel plate rheometry. Both authors contributed to analyzing the data, modeling the results, and preparing the manuscript. Both authors read and approved the final manuscript.

Funding
This work was supported by JSPS KAKENHI Grant Numbers JP18740272, JP21654068, JP15K13591, JP17H05417, JP18K03800.

Availability of data and materials
The data obtained in this study are available from IS upon request.

Declarations

Competing interests
The authors declare that they have no competing interests.

Received: 16 January 2022 Accepted: 30 July 2022
Published online: 12 August 2022

References

Allen JRL (1985) Principles of physical sedimentology. The Blackburn Press, Caldwell, New Jersey
Andreotti D, Forterre Y, Pouliquen O (2013) Granular media: between fluid and solid. Cambridge University Press, Cambridge
Araiba K, Suemine A (1998) In situ measurements of internal earth pressure during landslide movement. Soils Found 38:97–107
Askarinejad A, Akca D, Springman SM (2018) Precursors of instability in a natural slope due to rainfall: a full-scale experiment. Landslides 15:1745–1759. https://doi.org/10.1007/s10346-018-0994-0
Bartelt P, Vera Valero C, Feistl T, Christen M, Bühler Y, Buser O (2015) Modelling cohesion in snow avalanche flow. J Glaciol 61:837–850. https://doi.org/10.3189/2015JoG14J126
Bear J (1972) Dynamics of fluids in porous media. American Elsevier, New York
Berhanu M, Petroff A, Devauchelle O, Kudrolli A, Rothman DH (2012) Shape and dynamics of seepage erosion in a horizontal granular bed. Phys Rev E 86:041304. https://doi.org/10.1103/PhysRevE.86.041304
Bodó B, Jones C (2013) Introduction to soil mechanics. Wiley, West Sussex
Bozzano F, Cipriani I, Mazzanti P, Prestininzi A (2014) A field experiment for calibrating landslide time-of-failure prediction functions. Int J Rock Mech Min Sci 67:69–77. https://doi.org/10.1016/j.ijrmms/2013.12.006
Brackely IJA, Sanders PJ (1992) In situ measurement of total natural horizontal stresses in an expansive clay. Géotechnique 42:443–451
Carson MA (1971) The mechanics of erosion. Pion, London
Cislaghi A, Cohen D, Gasser E, Bischetti GB, Schwartz M (2019) Field measurements of passive earth forces in steep, shallow, landslide–prone areas. J Geophys Res Earth Surf 124:838–866. https://doi.org/10.1029/2017JF004557
De Blasio FB (2011) Introduction to the physics of landslides. Springer, Heidelberg. https://doi.org/10.1007/978-94-007-1122-8
Duran J (2000) Sands, powders, and grains: an introduction to the physics of granular materials, Japanese edition. Springer, New York (trans: Nakanishi H and Okumura K). Yoshioka, Kyoto
Fall A, Weber B, Pakpour M, Lenoir N, Shahidzadeh N, Fiscina J, Wagner C, Bonn D (2014) Sliding friction on wet and dry sand. Phys Rev Lett 112:175502. https://doi.org/10.1103/PhysRevLett.112.175502
Fox GA, Wilson GV (2010) The role of subsurface flow in hillslope and stream bank erosion: a review. Soil Sci Soc Am J 74:717–733. https://doi.org/10.2136/sssaj2009.0319
Fox GA, Wilson GV, Periketi RK, Cullum RF (2006) Sediment transport model for seepage erosion of streambank sediment. J Hydrol Eng 11:603–611. https://doi.org/10.1061/(ASCE)1084-0699(2006)11:6(603)
Fox GA, Chu-Agor ML, Wilson GV (2007) Erosion of noncohesive sediment by ground water seepage: lysimeter experiments and stability modeling. Soil Sci Soc Am J 71:1822–1830. https://doi.org/10.2136/sssaj2007.0090
Fredlund DG, Rahardjo H, Fredlund MD (2012) Unsaturated soil mechanics in engineering practice. Wiley, New York
Fukuoka M (1980) Landslides associated with rainfall. Geotech Eng 11:1–29
Fukuzono T (1985) A new method for predicting the failure time of a slope. In: Proceedings of IVth international conference and field workshop on landslides. Japan Landslide Society, Tokyo, pp 145–150
Gregoretti C, Maltauro A, Lanzoni S (2010) Laboratory experiments on the failure of coarse homogeneous sediment natural dams on a sloping bed. J Hydraul Eng 136:868–879. https://doi.org/10.1061/(ASCE)HY.1943-7900.0000259
Hayashi K, Sumita I (2017) Low-velocity impact cratering experiments in granular slopes. Icarus 291:160–175. https://doi.org/10.1016/jicarus.2017.03.027
Highland LM, Bobrowsky P (2008) The landslide handbook—a guide to understanding landslides. U.S.Geological Survey Circular 1325, Reston
Intrieri E, Carlà T, Gigli G (2019) Forecasting the time of failure of landslides at slope-scale: a literature review. Earth Sci Rev 193:333–349. https://doi.org/10.1016/j.earscirev.2019.03.019
Iverson RM (1997) The physics of debris flows. Rev Geophys 35:245–296
Iverson RM (2015) Scaling and design of landslide and debris-flow experiments. Geomorphology 244:9–20. https://doi.org/10.1016/j.geomorph.2015.02.033
Iverson RM, Reid ME, LaHusen RG (1997) Debris-flow mobilization from landslides. Annu Rev Earth Planet Sci 25:85–138
Iverson RM, Reid ME, Iverson NR, LaHusen RG, Logan M, Mann JE, Brien DL (2000) Acute sensitivity of landslide rates to initial soil porosity. Science 290:513–516. https://doi.org/10.1126/science.290.5491.513

Kamiisi I, Machida T, Oda K, Yamaguchi S, Sato A (2009) Measurement of cohesion and internal friction angle of wet snow [abstract (in Japanese)]. In: Summaries of JSSI & JSSE joint conference on snow and ice research. https://doi.org/10.14851/jcsir.2009.0.232.0
Krahn J, Fredlund DG, Klassen MJ (1989) Effect of soil suction on slope stability at Notch Hill. Can Geotech J 26:269–278
Lobkovsky AE, Jensen B, Kudrolli A, Rothman DH (2004) Threshold phenomena in erosion driven by subsurface flow. J Geophys Res 109:04010. https://doi.org/10.1029/2004JF000172
Matsukura Y (2008) Mass movements in rock and soil masses. University of Tsukuba Press, Tsukuba (in Japanese)
Matsushi Y, Matsukura Y (2006) Cohesion of unsaturated residual soils as a function of volumetric water content. Bull Eng Geol Environ 65:449–455. https://doi.org/10.1007/s10064-005-0035-9
Mavko G, Mukerji T, Dvorkin J (2019) The rock physics handbook, 3rd edn. Cambridge University Press, Cambridge. https://doi.org/10.1017/9781108333016
McKenzie D (1984) The generation and compaction of partially molten rock. J Petrol 25:713–765
Melosh HJ (2011) Planetary surface processes. Cambridge University Press, Cambridge
Mitarai N, Nori F (2006) Wet granular materials. Adv Phys 55:1–45. https://doi.org/10.1080/00018730600626065
Morimoto R, Nakamura K, Tsuneishi Y, Ossaka J, Tsunoda N (1967) Landslides in the epicentral area of Matsushiro earthquake swarm—their relation to the earthquake fault. Bull Earthq Res Inst 45:241–263
Moriwaki H, Inokuchi T, Hattanji T, Sassa K, Ochiai H, Wang G (2004) Failure processes in a full-scale landslide experiment using a rainfall simulator. Landslides 4:277–288. https://doi.org/10.1007/s10346-004-0034-0
Nowak S, Samadani A, Kurdolli A (2005) Maximum angle of stability of a wet granular pile. Nat Phys 1:50–52. https://doi.org/10.1038/nphys106
Okeke AC-U, Wang F (2016) Critical hydraulic gradients for seepage-induced failure of landslide dams. Geoenviron Disasters 3:9. https://doi.org/10.1186/s40677-016-0043-z
Orense RP, Shimoma S, Maeda K, Towhata I (2004) Instrumented model slope failure due to water seepage. J Nat Disaster Sci 26:15–26
Petley DN, Bulmer MH, Murphy F (2002) Patterns of movement in rotational and translational slides. Geology 30:719–722
Petley DN, Higuchi T, Petley DJ, Bulmer MH, Carey J (2005) Development of progressive landslide failure in cohesive materials. Geology 33:201–204. https://doi.org/10.1130/G21147.1
Scheel M, Seemann R, Brinkmann M, Di Michiel M, Sheppard A, Breidenbach B, Herminghaus S (2008) Morphological clues to wet granular pile stability. Nat Mater 7:189–193. https://doi.org/10.1038/nmat2117
Strauch S, Herminghaus S (2012) Wet granular matter: a truly complex fluid. Soft Matter 8:8271. https://doi.org/10.1039/c2sm25883h
Takita H, Sumita I (2013) Low-velocity impact cratering experiments in a wet sand target. Phys Rev E 88:022203. https://doi.org/10.1103/PhysRevE.88.022203
Terzaghi K, Peck RB, Mesri G (1996) Soil mechanics in engineering practice, 3rd edn. Wiley, New York
Tohari A, Nishigaki M, Komatsu M (2007) Laboratory rainfall-induced slope failure with moisture content measurement. J Geotech Geoenviron Eng 133:575–587. https://doi.org/10.1061/(ASCE)1090-0241(2007)133:5(575)
Turcotte DL, Schubert G (2014) Geodynamics, 3rd edn. Cambridge University Press, Cambridge
Varnes DJ (1978) Slope movement types and processes. Landslides: analysis and control, vol 176. Transportation Research Board Special Report, Washington, DC, pp 11–33
Voight B (1988) A method for prediction of volcanic eruptions. Nature 332:125–130
Voight B (1989) A relation to describe rate-dependent material failure. Science 243:200–203
Watts KS, Charles JA (1988) In situ measurement of vertical and horizontal stress from a vertical borehole. Géotechnique 38:619–626
Whitely JS, Chambers JE, Uhlemann S, Wilkinson PB, Kendall JM (2019) Geophysical monitoring of moisture-induced landslides. Rev Geophys 57:106–145. https://doi.org/10.1029/2018RG000603

Publisher's Note